

Morphological features and water solubility of iron in aged fine aerosol particles over the Indian Ocean

Sayako Ueda¹, Yoko Iwamoto², Fumikazu Taketani³, Mingxu Liu¹, Hitoshi Matsui¹

5 ¹ Graduate School of Environmental Studies, Nagoya University, Nagoya, 464-8601, Japan

² Graduate School of Integrated Sciences for Life, Hiroshima University, Hiroshima University, Higashi-Hiroshima, 739-8521, Japan

³ Japan Agency for Marine-Earth Science and Technology, Yokohama, 237-0061, Japan

Correspondence to: Sayako Ueda (ueda.sayako.u2@f.mail.nagoya-u.ac.jp)

Abstract. Atmospheric transport of iron (Fe) in fine anthropogenic aerosol particles is an important route of soluble Fe supply from continental areas to remote oceans. To investigate Fe properties of aerosol particles over remote oceans, we analyzed atmospheric aerosol particles over the Indian Ocean during the research vessel Hakuho Maru KH-18-6 cruise. **Aerosol particles were collected using a cascade impactor. Particles on the sample stage of 0.3–0.8 μm aerodynamic diameter were analyzed using transmission electron microscopy (TEM) with an energy-dispersive X-ray spectrometry analyzer.** The particle shape and composition indicated that most particles collected north of the equator were composed mainly of ammonium sulfate. Regarding the particle number fraction, 0.6–3.0% of particles contained Fe, which mostly co-existed with sulfate. Of those particles, 26% of Fe occurred as metal spheres, often co-existing with Al or Si, regarded as fly ash, 14% as mineral dust, and 7% as iron oxide aggregations. Water-dialysis analyses of TEM samples indicated that Fe in spherical fly ash was almost entirely insoluble, whereas Fe in the other morphological-typed particles was partly (65% Fe mass on average) soluble. Global model simulations mostly reproduce observed Fe mass concentrations in $\text{PM}_{2.5}$ collected using a high-volume air sampler, including their north–south contrast during the cruise. In contrast, a marked difference was found between the simulated mass fractions of Fe mineral sources and the observed Fe types. For instance, the model underestimated anthropogenic aluminosilicate Fe contained in matter such as fly ash from coal combustion. Our observations suggest that Fe in particles over remote ocean areas has multiple shapes and minerals, and further suggest that its solubility after aging processes differs depending on their morphological and mineral type. Proper consideration of such Fe types at their sources is necessary for accurate estimation of atmospheric Fe effects on marine biological activity.

30

1 Introduction

Iron (Fe) is recognized as an essential micronutrient for ocean primary productivity. Addition of water-soluble Fe to remote oceans, designated as a high-nutrient and low-chlorophyll region, stimulates phytoplankton blooms. Iron can thereby change the marine environment and biological diversity, and the global carbon cycle (Martine and Fitzwater, 1988; Baar et al., 1995; Harrison et al., 1999; Jickells et al., 2005; Tsuda et al., 2003 and 2007; 35 Iwamoto et al., 2009). Transport and deposition of atmospheric aerosol particles is an important route supplying Fe to remote ocean areas. Main sources of soluble Fe in the atmosphere are Fe-containing mineral dust and Fe emitted from anthropogenic combustion and biomass burning (combustion Fe) (e.g. Guieu et al., 2005; Mahowald et al., 2009). Mineral dust is emitted mainly as coarse particles by dust storms occurring in arid and 40 semi-arid continental areas. By contrast, combustion Fe is emitted as both fine and coarse particles, through evaporation and condensation processes (Markowski and Filby, 1985; Liu et al., 2018; Ohata et al., 2018). Although many earlier studies have implicated mineral dust as an important source of soluble Fe to oceans (e.g. Uematsu et al., 1893; Mahowald et al., 2005; Iwamoto et al., 2011), anthropogenic Fe has also attracted increasing attention recently as a source supplying water-soluble Fe, steadily and efficiently, by long-range 45 transport (Chuang et al., 2005; Sedwick et al., 2007; Luo et al., 2008; Takahashi et al., 2013; Ito, 2015; Matsui et al., 2018b).

Recent sophisticated global aerosol modeling studies have evaluated global climatic effects of anthropogenic Fe (e.g., Scanza et al., 2018; Matsui et al., 2018b; Rathod et al., 2020). Matsui et al. (2018b) demonstrated that the atmospheric burden of anthropogenic combustion Fe is eight times greater than earlier estimates had 50 suggested. Simulation using a soluble Fe mechanism designed for Earth system models by Scanza et al. (2018) incorporates consideration of changes of Fe solubility with atmospheric processing of Fe in dust and combustion aerosols. They concluded that, in many remote ocean regions, sources of Fe from combustion and dust aerosols are equally important. Moreover, Rathod et al. (2020) released a revised emission inventory of anthropogenic combustion Fe using a technology-based methodology. However, the accuracy of current model-based estimates

55 remains unclear because of the lack of information related to the mineral composition, morphological structure, and solubility of actual Fe-containing particles in the atmosphere, especially in remote ocean areas.

Actually, Fe is emitted as aerosol particles having various morphologies, with their mineralogy and size distributions according to their sources. Particle size and composition are related to the particle lifetime and water-solubility of Fe. In addition, changes of Fe solubility with particle aging processes depend on many factors
60 such as Fe mineralogy and size, atmospheric and meteorological conditions, and particle acidity (Wiederhold et al., 2006; Journet et al., 2008; Cwiertny et al., 2008; Shi et al., 2009 and 2015; Ito and Feng, 2010; Li et al., 2017; Sakata et al., 2022). Earlier knowledge about relations between solubility, Fe mineral species, and aging processes has usually been based on bulk sample measurements, laboratory experiments, and simulations. However, information about individual Fe-containing particles that have experienced actual atmospheric
65 transport remains insufficient. To evaluate model results, Fe mass concentrations and solubilities measured during numerous observation studies and chemical analyses of bulk samples have been used (Mahowald et al., 2009; Wang et al., 2015; Myriokefalitakis et al., 2018; Rathod et al. 2020). Nevertheless, data of bulk samples alone do not provide information about the source, mineralogy, atmospheric aging, or solubility of individual Fe-containing particles. Enhancing our understanding of the roles and effects of atmospheric Fe on marine
70 environments necessitates the elucidation of details of atmospheric Fe properties in remote areas far from their sources.

Compared to major aerosols such as sea-salt and sulfates, Fe-containing particles constitute a minority in remote areas. This relative scarcity makes it difficult to find and investigate Fe-containing particles in aerosol samples. However, some observation studies conducted in leeward areas of polluted regions have revealed trace
75 metals in individual particles (Hidemori et al., 2014; Li et al., 2017). For example, Li et al. (2017) investigated individual Fe-containing particles aged for 1–2 days using single-particle analysis of samples collected under polluted air over the East China Sea. Using scanning transmission electron microscopy (STEM) and nanoscale secondary ion mass spectrometry, they demonstrated the presence of iron sulfate in a sulfate coating around

iron oxide (FeO_x) as evidence of Fe aging. Sample collection leeward of polluted regions and recent microscopic
80 techniques have made it possible to find minor Fe in aged particles. As a technique of microscopic analysis,
water dialysis is a powerful tool for the investigation of the ratio of water soluble and insoluble materials in
individual particles (Okada et al., 1983; Miki et al., 2014; Ueda et al., 2011ab, 2018, 2022). This method
comprises morphological observations and comparison before and after water dialysis of aerosols. Combination
with energy-dispersive X ray spectrometry (EDS) can quantify water-soluble elements in individual particles
85 (Ueda et al., 2022).

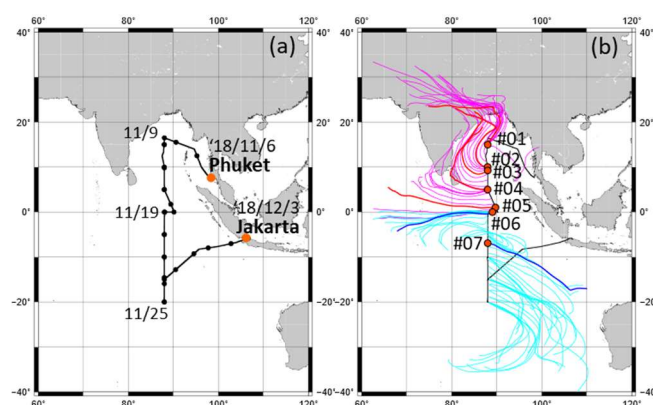
For this study, we conducted sampling to investigate aged Fe-containing particles onboard the R/V Hakuho
Maru KH-18-6 cruise of November 2018 over the Indian Ocean. South Asian regions have severe air pollution
problems even now, attributable to anthropogenic and natural sources (Gyttukunda et al., 2014; Chen et al.,
2020; Dhaka et al., 2020; Kanawade et al., 2020; Ojha et al., 2020; Takigawa et al., 2020). Sea areas around the
90 KH-18-6 cruise shipping route are not areas with Fe limitations on primary production by marine
microorganisms (Mahowald et al., 2018), but are suitable for catching aerosols in long-range transported
polluted air from South Asia. Using transmission electron microscopy (TEM) analysis with EDS and water
dialysis in this study specifically examining samples of fine particles that can contain combustion aerosols, we
investigated morphological features of Fe-containing particles related to the origin and atmospheric aging
95 process. As basic data for aerosols, bulk aerosol sampling of $\text{PM}_{2.5}$ was conducted to measure ions and metals.
After describing the methods (Sect. 2), this paper presents the mass concentration and number fraction of Fe
and their relation with other major aerosol components internally and externally co-existing with Fe, based on
analyses of bulk samples and TEM observations (Sects. 3.1 and 3.2). Then, typical morphological features of
Fe-containing particles are explained in terms of their relation to the Fe source (Sect. 3.3). Additionally, this
100 report describes global model simulations of each source Fe and comparison with results obtained from
observations (Sect. 3.4). Finally, differences of measured solubility for morphologically categorized Fe are

presented with discussion of their relation to atmospheric aging, along with implications from these simulations of Fe (Sect. 3.5).

2 Methods

105 2.1 Atmospheric observations on board and air mass backward trajectories

Atmospheric observations were conducted over the Indian Ocean during the R/V *Hakuho Maru KH-18-6* cruise, which took place on 6–28 November 2018. Figure 1 portrays ship tracks of the R/V *Hakuho Maru* cruise, 5-day backward air mass trajectories, and sampling locations of TEM samples. The backward trajectories were computed using the Hybrid Single-Particle Lagrangian Integrated Trajectory (HYSPLIT) model developed by the National Oceanic and Atmospheric Administration (NOAA) Air Resources Laboratory (ARL) (Stein et al., 2015; Rolph et al., 2017). The settings of the trajectory duration, starting height, vertical mode calculation method, and dataset were chosen, respectively, as 5 days, 500 m above sea level, model vertical velocity, and GDAS meteorological data. Air masses of the northern Indian Ocean (6–16 November 2018) originated from India. Those around the equator arrived from the east (6–19 November 2018); those of the southern Indian Ocean were from the sea around western Australia, moving counterclockwise to the observation sites (20–28 November 2018).



120 **Figure 1: Ship tracks of KH-18-06 cruise of the R/V Hakuho Maru (a) and 5-day horizontal backward air mass trajectory (b). Black dots of (a) represent 0:00 am of each day at universal time. Calculations of backward air mass trajectory started from 500 m a.s.l., above the site. Magenta and cyan thin lines respectively show trajectories of every 6 h for sites north and south of the equator. Orange circles of (b) represent TEM sampling sites. Red and blue lines show trajectories for TEM sampling.**

2.2 Chemical composition of PM_{2.5}

125 We collected PM_{2.5} samples on Teflon filters (WP500-50; Sumitomo Electric Fine Polymer, Inc.) and prebaked (900 °C for 3 h) quartz fiber filters (QR-100; Advantec Toyo Kaisha Ltd.) using two high-volume samplers (HV-700F; Shibata Science Co. Ltd.) with a custom-made particle-size separator at about 12-h or 24-h intervals at a flow rate of 500 L min⁻¹ on the compass deck (a.s.l. 14 m). To avoid collecting particles from the ship exhaust (the ship's funnel was located to the rear of the sampling position), the pumping of aerosol samplers

130 was controlled automatically using a wind sector to operate only when the relative wind direction was -80° to 80° of the bow and when the relative wind speed was higher than 3 m s⁻¹. After collection, the Teflon and quartz fiber filter samples (for ionic species and trace metals) were stored at the home laboratory before chemical analyses, respectively at 4 °C and -18 °C. Mass concentrations of water-soluble ionic species (Cl⁻, NO₃⁻, SO₄²⁻, Na⁺, NH₄⁺, K⁺, Mg²⁺, and Ca²⁺) on quartz fiber filter samples (12 samples collected during 8–28 November

135 2018) were analyzed using ion chromatography. Non-sea-salt (nss) concentrations of SO₄²⁻, K⁺, and Ca²⁺ were

estimated from Na^+ concentrations in the samples using the bulk seawater ratios described by Wilson (1975). Metals in $\text{PM}_{2.5}$ (Na, Al, K, Ca, Ti, V, Mn, Fe, Ni, and Zn) were analyzed using inductively coupled plasma mass spectrometry (ICP-MS, 7700X, G3281A; Agilent Technologies, Inc.) with microwave-assisted extraction in a mixture of nitric acid, hydrofluoric acid, and hydrogen peroxide using the Teflon filter sample (14 samples collected during 8–30 November 2018).

2.3 Individual particle analyses using an electron microscope

2.3.1 Observation and elemental analysis

Aerosol particles were collected for morphological particle analysis using TEM. Aerosols after diffusion drying were collected on carbon-coated nitrocellulose (collodion) films using cascade impactors. The 50% cut-off diameters of the three stages 1, 2, and 3 were, respectively, 1.6 μm , 0.8 μm , and 0.3 μm . Aerosol samples were collected at the upwind side on the compass deck of the ship for 10–30 min at a flow rate of 1.0 L min^{-1} . About 1–2 TEM samples were taken per day and were stored under dry conditions at room temperature (about 25°C) until TEM analyses were conducted at Nagoya University. For this study, seven samples (#01–07) of stage 3 were used for analyses. Sample collection sites and the 5-day backward trajectories are depicted in Fig. 1b. Sample details are presented in Table 1.

Table 1: TEM samples used for this study and analyzed particle and Fe-containing particle numbers

Sample ID	Sampling time		Location		Atmospheric conditions		EDS analyzed particles	Fe-containing particles	
	start time	period	Lat.	Long.	Temp.	RH		number	%
	YYYY/MM/DD h:mm	min	N deg.	E deg.	°C	%	number	number	%
#01	2018/11/10 2:43	10	14.99	87.99	28.8	66	535	3	0.6
#02	2018/11/12 1:51	10	10.02	87.98	28.9	81	305	2	0.7
#03	2018/11/13 2:01	20	9.24	88.00	28.8	80	703	17	2.4
#04	2018/11/14 2:36	20	5.01	87.98	28.8	74	507	10	2.0
#05	2018/11/16 2:31	20	1.01	89.72	29.5	69	336	10	3.0
#06	2018/11/18 8:05	25	-0.01	89.06	32.3	60	136	2	1.5
#07	2018/11/21 7:56	31	-6.92	88.00	29.3	71	106	1	0.9

Particles collected on the collodion film were photographed using TEM (200 keV, JEM-2100 plus; JEOL
155 Ltd.) at $1.2 \text{ k} \times$ and $6 \text{ k} \times$ magnifications. To measure the heights of individual particles on the collection surface, particles were coated with a Pt/Pd alloy at a shadowing angle of 26.6° ($\arctan 0.5$) before being micrographed. The Pt/Pd coating thickness was about 7 \AA . The EDS analyses were conducted using the TEM operated in STEM mode at 200 keV. Similar analyses of TEM and EDS hyperspectral imaging (HSI) data were described by Ueda et al. (2020 and 2022) and by Ueda (2021). For this study, EDS-HSI data were sampled at greater than
160 20 k magnification for 10–30 frames (20 s per frame) and were kept for each dot of 256×256 pixels using software (NSS3; Thermo Fisher Scientific Inc., Hampton, NH, USA). The dot size was $26 \times 26 \text{ nm}$ in the observed field at 20 k magnification. Although estimation of the mass of each element from EDS analysis is difficult, software can estimate the mass fraction (MF_X) of an element X to all analyzed elements from

measurement results of X-ray counts as values relative to detected elements. Elemental analyses were conducted
165 fundamentally for C, N, O, Na, Mg, Al, Si, P, S, Cl, K, Ca, Ti, V, Mn, Fe, Cu, Zn, Pd, and Pt. Although the
software can identify another element automatically if EDS spectra have a specific X-ray peak, other elements
were detected only rarely. The X-ray count sensitivity when detected using an EDS analyzer depends on the
analytical conditions, such as the frame number for analyses and adjustment of the electron beam and detector.
Because some conditions can change, evaluating X-ray count values as absolute values is difficult for samples
170 analyzed on different days or at different settings. Although estimating the mass of each element is not possible,
analyzing EDS spectra using software can estimate the mass fraction (MF) of each element from measurement
results of X-ray counts as values relative to the selected elements. The mass fraction of element X is described
as shown below.

$$MF_X = \frac{m_X}{m_{total}} \quad (1)$$

175 Therein, m_X and m_{total} respectively represent the mass of an element X in a selected area and the mass of all
analyzed (selected) elements in the area. For this study, TEM samples before water dialysis were coated
uniformly by Pd/Pd using the shadowing method. Pd is not included in general aerosols. In addition, samples
#01–07 were vapor-deposited by Pt/Pd at one time. Therefore, the MF_X value standardized by MF_{Pd} , X/Pd , can
be treated as a value that is independent from m_{total} , which changes according to the aerosol composition,
180 collodion film thickness, and distance from the Cu grid.

$$X/Pd = \frac{MF_X}{MF_{Pd}} = \frac{m_X}{m_{Pd}} \quad (2)$$

To obtain the elemental compositions of individual particles, the MF_X of each element was obtained manually
for selected areas according to the particle shape and size of each. Noise effects of the background were also
eliminated using X/Pd . If the difference of the X/Pd value of a particle area to that of a near background area
185 was greater than three standard deviations of multiple background spectra in the same sample, then the value
was treated as a significant spectrum of the particle.

2.3.2 Water dialysis and estimation of water-soluble Fe fraction (f_{WSFe})

For samples collected from the Indian Ocean (samples #01–#05) north of the equator, a water dialysis technique (Mossop, 1963; Okada, 1983; Okada et al., 2001; Ueda et al., 2011ab, 2018, 2022) was applied to observe and estimate the volume fraction of water-soluble and insoluble materials in particles. The TEM grid with particle samples was floated on an ultrapure water drop (~0.3 ml) on a petri dish at about 25°C for 3 h with the collection side upward. After water dialysis, some areas were photographed again. Unfortunately, a large part of the collodion film tore during water dialysis. For sample #03 only, some EDS analysis data for Fe-containing particles were obtained from the same particle area after water dialysis.

For this study, we expanded the water dialysis technique and EDS analysis to quantify changes of the fraction of water-soluble Fe to total Fe in individual Fe-containing particles. Because Pd is a water-insoluble material coated on the top surface of samples in this study, the mass of Pd for a selected area after water dialysis (m_{Pd_after}) can be regarded as equivalent to that for the same area before water dialysis (m_{Pd_before}).

$$m_{Pd_before} = m_{Pd_after} \quad (3)$$

The fraction of water-insoluble Fe (WIFe) mass to the total Fe mass in a particle, f_{WIFe} , can be represented as

$$f_{WIFe} = \frac{m_{WIFe}}{m_{Fe}} \times 100 [\%] = \frac{m_{Fe_after}}{m_{Fe_before}} \times 100 [\%], \quad (4)$$

where m_{Fe_before} and m_{Fe_after} respectively denote the Fe mass before and after water dialysis for a Fe-containing particle. Under equation (3), equation (4) can be described using Fe/Pd before and after water dialysis of the same area for a Fe-containing particle (respectively, Fe/Pd_{before} and Fe/Pd_{after}), which are based only on measurable values.

$$f_{WIFe} = \frac{Fe/Pd_{after}}{Fe/Pd_{before}} \times 100 [\%] \quad (5)$$

Finally, the fraction of water-soluble Fe to total Fe in a particle, f_{WSFe} can be estimated as presented below.

$$f_{WSFe} = 100 - f_{WIFe} [\%] \quad (6)$$

210 2.4 Global model simulation of Fe

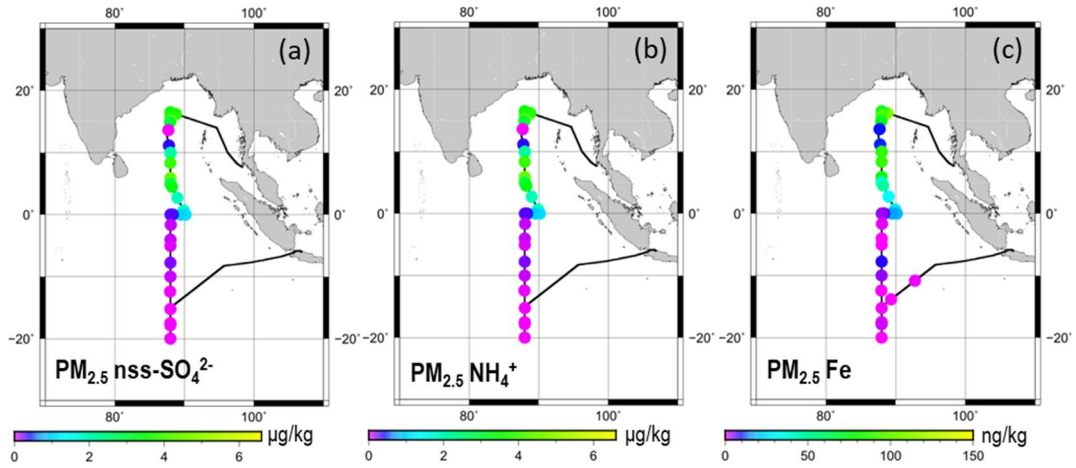
We conducted global model simulations using the Community Atmosphere Model (ver. 5; CAM5) with the Aerosol Two-dimensional bin module for foRmation and Aging Simulation (ver. 2; CAM5-chem/ATRAS2), with modifications for particulate iron (Matsui et al., 2014, 2018a; Matsui and Mahowald, 2017; Matsui, 2017; Liu and Matsui, 2021a, 2021b; Liu et al., 2022). Model setting for this study was described by Liu et al. (2022).
215 Briefly, the model incorporates emissions, gas-phase chemistry, condensation or evaporation of inorganic and organic species, coagulation, nucleation, activation of aerosols and evaporation from clouds, aerosol formation in clouds, dry and wet deposition, aerosol optical properties, aerosol–radiation interactions, and aerosol–cloud interactions. Aerosol particles were resolved with 12 size bins from 0.001 to 10 μm dry diameter. The model was run with horizontal resolution of $1.9^\circ \times 2.5^\circ$ and 30 vertical layers from the surface to approximately 40 km.
220 The near-surface layer of model results was used for this study.

The model explicitly treats Fe from biomass burning and anthropogenic combustion. Five Fe sources/minerals (biomass burning, and four anthropogenic Fe (magnetite (Fe_3O_4), hematite (Fe_2O_3), kaolinite ($\text{Al}_2\text{Si}_2\text{O}_5(\text{OH})_4$) and illite ($(\text{K}, \text{H}_3\text{O})(\text{Al}, \text{Mg}, \text{Fe})_2(\text{Si}, \text{Al})_4\text{O}_{10}$)) are considered in addition to eight other aerosol species: sulfate, nitrate, ammonium, dust, sea salt, primary and secondary organic aerosol, BC, and water. The
225 anthropogenic Fe emission inventory developed by Rathod et al. (2020) with the update by Liu et al. (2022) for southern Africa was used to model global-scale atmospheric iron concentrations. The size distribution of anthropogenic Fe was referred from observation results reported by Moteki et al. (2017) for magnetite over eastern Asia from aircraft measurements using a single-particle soot photometer. Combustion iron emissions from open biomass burning were calculated based on Luo et al. (2008). Dust Fe was not treated in our model,
230 but we assumed a constant iron content of 3.5% in natural dust (Duce et al., 1991; Jickells et al., 2005; Shi et al., 2012).

3 Results and Discussion

3.1 Horizontal variation of PM_{2.5} components

Figure 2 shows horizontal distributions of the mass concentrations of nss-SO₄²⁻, NH₄⁺, and Fe in PM_{2.5}. The values are shown as mass mixing ratios (measured mass concentration divided by the atmospheric density [1.18–1.21 kg/m³] calculated using the daily average of temperature and atmospheric pressure measured on board), with the same unit of model output, as discussed later (section 3.4). On average, the 25th percentile and the 75th percentile mass concentrations of ions and metals north and south of the equator at 87–90°E are presented respectively in Tables 2 and 3. Scatter plots showing concentrations of Fe and the other elements are presented in Figs. S1 and S2 of Supplemental Materials. Among the measured ions in PM_{2.5}, the sum of the mass fractions of nss-SO₄²⁻, NH₄⁺, Na⁺, and Cl⁻ was larger than 84% of the total ion mass concentration. North of the equator, nss-SO₄²⁻ and NH₄⁺ concentrations were especially high. These mass fractions were, respectively, 70–76% and 18–22%, except for data of 11 November 2018, when rain events occurred. The values of nss-K⁺, also tended to be north of the equator. Actually, nss-K⁺ in fine particles have often been regarded as a tracer of biomass burning (Andreae, 1983; Kawamura and Kaplan, 1987; Narukawa et al., 1999). High fire counts and pollution, such as by crop residue burning, have also been reported around northern India from October through November (Bray et al., 2019; Shaik et al., 2019). Therefore, the nss-K⁺ concentration of north site in this study might be affected somewhat by biomass burning around the windward continental area. South of the equator, the nss-SO₄²⁻ and NH₄⁺ concentrations were lower. Consequently, the fractions of sea salt components (i.e. Na⁺ and Cl⁻) increased. The PM_{2.5} ionic amounts in equivalent concentrations of total cation without H⁺ were comparable to or greater than 75% of that of total anion (Fig. S1a). For non-sea-salt components, the relations between the doubled nss-SO₄²⁻ molar concentration and the NH₄⁺ plus nss-K⁺ molar concentration were usually between 1:1 and 2:1 (Fig. S1b), suggesting that nss-SO₄²⁻ originated from ammonium sulfate, ammonium bisulfate, and potassium sulfate rather than from sulfuric acid.



255

Figure 2: Horizontal variation of mass concentrations of (a) $nss-SO_4^{2-}$, (b) NH_4^+ , and (c) Fe in $PM_{2.5}$. Each sample was collected continuously 12 h or 24 h under controlling by wind sector. Data are as shown at averaged locations for latitude and longitude during the sampling period.

Table 2: Average values of PM_{2.5} ion mass concentrations at 87–90°E

	0–16°N	0–20°S
	µg/g	µg/g
Cl ⁻	0.04 [0.02–0.03]*	0.17 [0.02–0.25]*
NO ₃ ⁻	0.05 [0.03–0.08]*	0.05 [0.03–0.06]*
SO ₄ ²⁻	11 [7.1–16]*	1.3 [0.39–1.4]*
Na ⁺	0.19 [0.16–0.23]*	0.18 [0.07–0.30]*
NH ₄ ⁺	3.2 [1.9–4.1]*	0.26 [0.02–0.29]*
K ⁺	0.45 [0.16–0.66]*	0.04 [0.01–0.05]*
Mg ²⁺	0.03 [0.03–0.04]*	0.02 [0.01–0.03]*
Ca ²⁺	0.06 [0.04–0.07]*	0.04 [0.03–0.05]*
nss-SO ₄ ²⁻	11.0 [7.0–16.1]*	1.2 [0.3–1.4]*
nss-K ⁺	0.44 [0.16–0.65]*	0.03 [0.00–0.05]*
nss-Ca ²⁺	0.05 [0.03–0.07]*	0.03 [0.02–0.05]*

260 * Values in square brackets indicate 25th and 75th percentile value ranges.

Table 3: Average values of PM_{2.5} metal mass concentration at 87–90°E

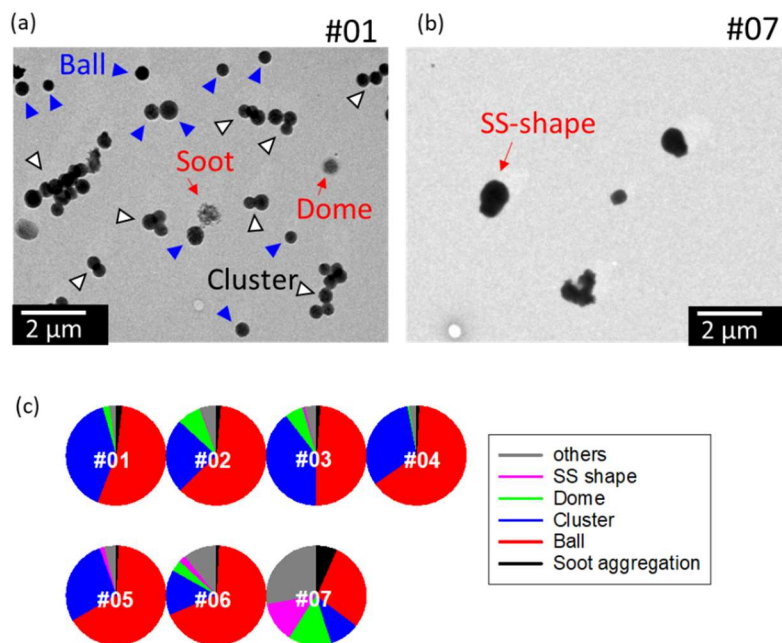
	0–16°N	0–20°S
	ng/g	ng/g
Na	307 [232–378]*	221.6 [73–349]*
Al	119 [48–139]*	13 [0.0–27]*
K	446 [164–467]*	39 [7.1–59]*
Ca	37 [17–42]*	7.9 [4.6–12.4]*
Ti	5.0 [1.9–6.2]*	0.3 [0.0–0.5]*
V	1.6 [0.7–1.9]*	0.4 [0.0–0.6]*
Fe	67 [27–86]*	4.3 [0.1–6.7]*
Ni	0.7 [0.3–0.8]*	0.1 [0.0–0.2]*
Zn	67 [28–72]*	3.2 [0.0–3.6]*

* Values in square brackets are 25th and 75th percentile value ranges.

Among metals measured using ICP-MS, the Na and K mass concentrations were high (71–1280 ng m⁻³ and 6–1210 ng m⁻³, respectively). The Fe concentrations were high (31–162 ng m⁻³) north of the equator, but low (<22 ng m⁻³) south of the equator. The Fe mass concentrations were well correlated positively with nss-K⁺ ($R^2=0.95$), nss-SO₄²⁻ ($R^2=0.93$), and Ca ($R^2=0.90$) mass concentrations (Fig. S2). The concentrations of V and Ni, which originate from heavy oil combustion by ships, were correlated closely (R^2 of 0.96). However, their correlations with Fe concentration (R^2 values of 0.69 and 0.83, respectively) were weaker than the correlation between V and Ni or the correlations of Fe found with nss-K⁺, nss-SO₄²⁻, and Ca. These results suggest that a large fraction of the observed Fe had been transported from around the continental atmosphere with dust, nss-K⁺, and nss-SO₄²⁻. However, the good correlation with continental elements implies that Fe was transported together with the continental air mass, but it does not imply that emission sources for each element are the same. Therefore, details of the composition and morphological features of individual Fe-containing particles were investigated as described in the following sections.

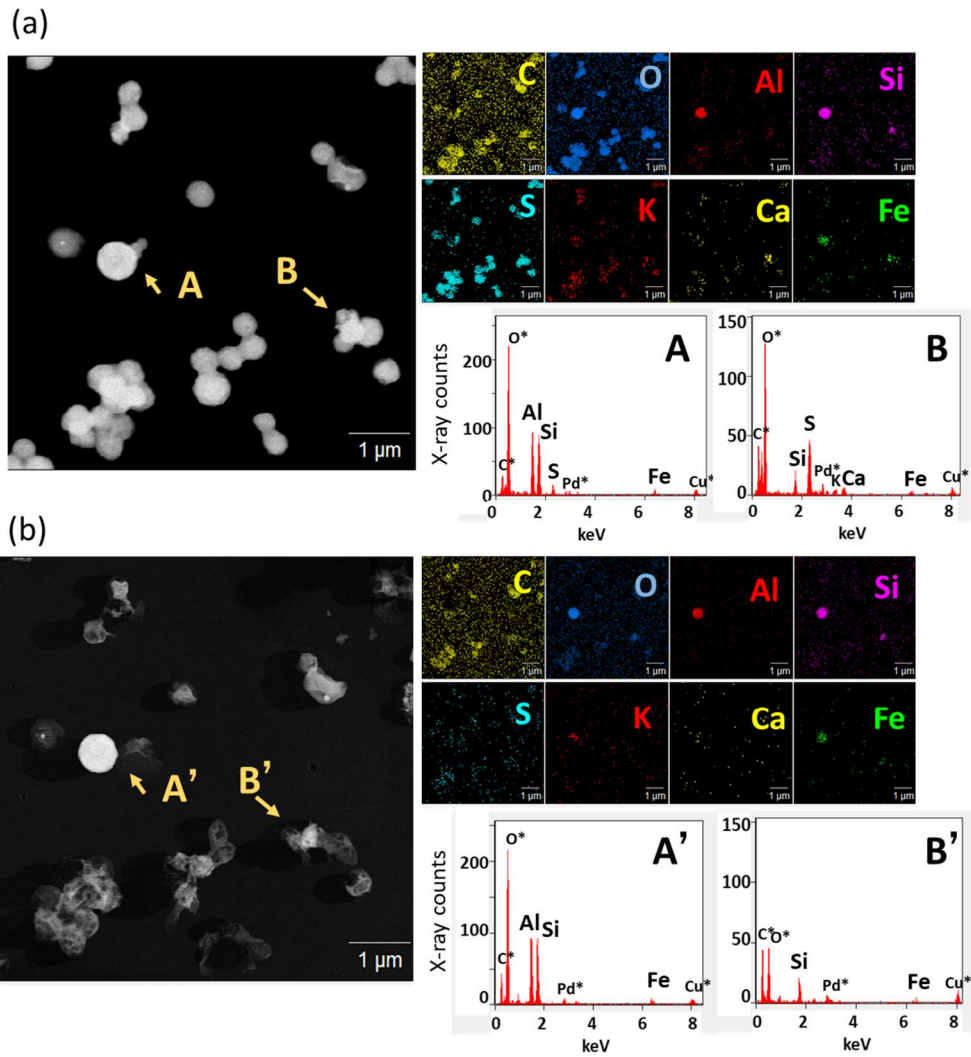
3.2 Individual particle features and co-existing states with Fe of sulfate and soot

Photographs of all samples (#01–07) are shown respectively as Fig. S3 of Supplemental Materials. Morphological features of samples #01–06 were similar. Electron microphotographs of samples #01 and #07 and number fractions of the morphological types for all samples are presented in Fig. 3. The morphological types were classified based on a report by Ueda et al. (2016) and features of particles on the samples. For samples #01–06, many particles in all samples had a rounded shape (ball) or were clustered into ball shapes (cluster), such as the blue and white arrowed particles of sample #01 of Fig. 3. Dome-shaped particles have less height to area (dome). Chain aggregation of small globules (ca. 30 nm) is regarded as a particle composed mainly of soot (soot), although they were a small fraction. For sample #07, some particles constructed of cubic parts having high contrast to an electron beam were also found. They can usually be regarded as sea salt (SS)-shaped.



290 **Figure 3: Electron micrographs for samples #01 (a) and #07 (b), and Pie chart showing the number fractions of morphological types (c). Blue arrowed particles are ball-like shaped particles. White arrowed particles are clusters of balls. Red arrows indicate soot, dome-shaped, and sea-salt (SS)-shaped particles.**

Figure 4a shows a STEM image and EDS mapping of C, O, Al, Si, S, K, Ca, and Fe of an area of sample #03 and examples of the X-ray count spectrum for each particle. Ball-like and clustered particles were composed mainly of S, C, and O, indicating sulfate with organics. K signals in the particles were often found at the same position as the detected S signal. Number fractions of particles detecting each element are depicted in Fig. 5. S was detected from >92% of all particles for samples collected north of the equator. K was detected from 16–44% particles. For other elements, particles containing sea salt (Na, Mg and Cl) were often detected (3–48% of all particles). In addition, Al and Si were detected in about 5% of particles collected north of the equator. Findings show that Fe was detected in 1–4% of all particles.



300

Figure 4: STEM image and an elemental map of sample #03 for the same region (a) before and (b) after water dialysis and extracted X-ray count spectrum for arrowed particles A and B and for the same region after water dialysis (A' and B'). Asterisk (*) elements represent elements included in the background area without particles.

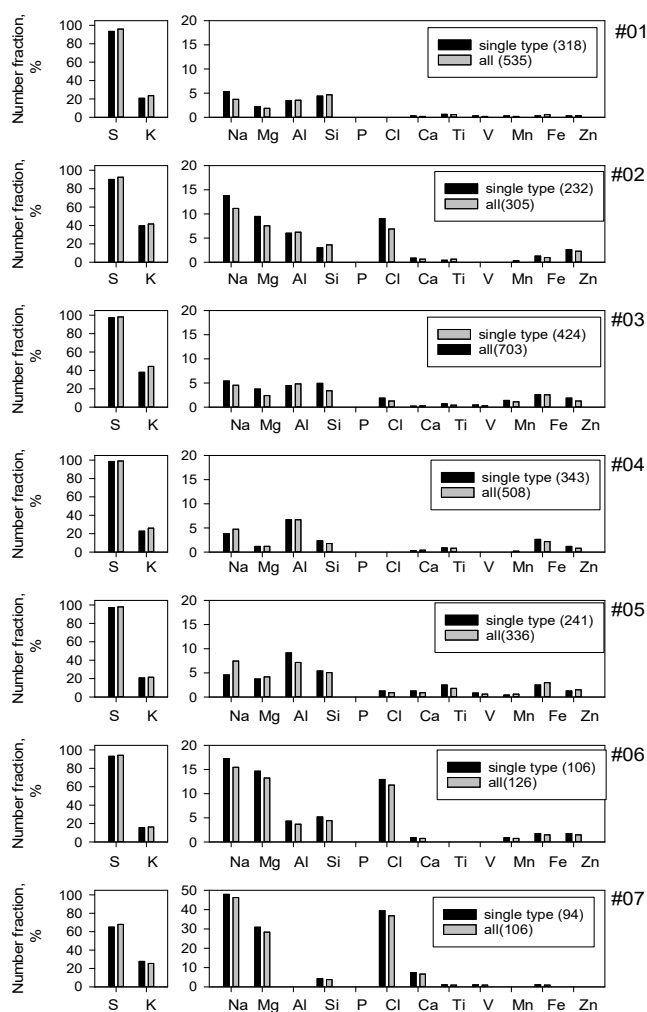


Figure 5: Number fractions of element-containing particles. Single type denotes particles except cluster-shaped particles. Bracketed numbers in the legend are analyzed particles.

As shown by particles A and B in Fig. 4a, Fe signals were often found from a partial area with attached or coated sulfate. For this study, metal-congested areas containing Fe are designated as Fe-containing parts, to distinguish a term from whole particles (Fe-containing particles) such as particles with a co-existing Fe-containing part and sulfate. From some Fe-containing parts, Si, Al and/or Ca were also detected. Compositions of Fe-containing particles and types of Fe-containing parts are detailed in the next section. Figure 4b shows a

STEM image, EDS mapping, and X-ray count spectra after water dialysis for the same area as that portrayed in Fig. 4a. A large part composed of S and K disappeared with dissolution by water dialysis, suggesting that they have hygroscopicity. However, many parts composed of Si, Al, Fe or C remained on film.

Co-existing Fe-containing parts and sulfate were found from TEM samples. Such particles are probably formed with secondary formation or coagulation of sulfate with an Fe-containing particle. Good correlation between Fe and SO_4^{2-} , as explained in Sect. 3.1, also suggests that a large mass of Fe was transported to the ocean with sulfate particles and their precursor gases. Relations of sulfate particle shapes on samples to their acidity have been reported from some earlier microscopic studies, as explained hereinafter. Acidic sulfate particles such as sulfuric acid (H_2SO_4) and bisulfate (NH_4HSO_4) are usually found as droplets having a satellite structure because of their property of retaining water even if they were collected after diffusion drying (Waller et al., 1963; Frank and Lodge, 1967; Gras and Ayers, 1979; Bigg, 1980; Ferek et al., 1983; Ueda et al., 2011b). By contrast, particles composed mainly of ammonium sulfate collected after passing the diffusion dryer have been found as ball-like rectangular, regular shapes or clusters (Ueda et al., 2011b; Ueda, 2021). Most particles on samples examined for this study, have a ball-like shape or a cluster. This result indicates that sulfates in the particles were more closely related to neutralized sulfate such as ammonium sulfate than to sulfuric acid, which also corresponds with the result found for $\text{PM}_{2.5}$, as shown in Sect. 3.1. Particles composed mainly of ammonium sulfate can be present as solid or liquid under their deliquescence humidity, according to atmospheric humidity experience. In addition, solid ammonium sulfate particles tend to change to rectangular regular shapes when experiencing a metastable humidity condition (Ueda, 2021). However, rectangular particles were rarely observed in this study, although the atmospheric relative humidity (60–81%RH) at the sampling time (Table 1) is usually a metastable condition of ammonium sulfate (35–80%RH). Therefore, sulfate particles in our samples presumably existed as droplet particles in the atmosphere.

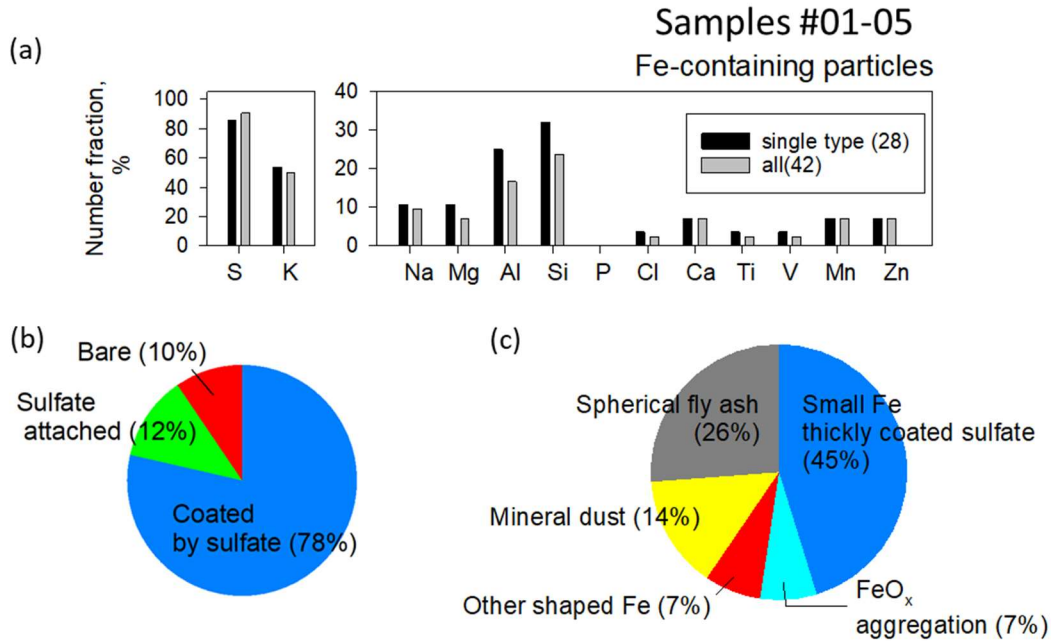
Based on reports of measurements of single soot mass analysis by Corbin et al. (2018), much soot originating from combustion of heavy fuel oil in ship engines can contain Fe addition to V, Na, and Pb. Some soot particles

that are less-coated by sulfate were also found from our samples. However, metals including Fe were not detected from less-coated soot particles in this study, as shown in Fig. S4. As reasons for the presence of less-coated soot over the remote ocean, it might be true that hydrophobic or less-coated soot preferentially survives in the atmosphere after transport (Ueda et al., 2018; Kompalli et al., 2021; Ueda et al., 2022) in addition to local ship's exhaust. For our PM_{2.5} result, as explained in Sect. 3.1, Fe was somewhat correlated with V, although the correlation was weaker than that between V and Ni, or those between Fe and either nss-SO₄²⁻, nss-K⁺ or Ca. Some Fe might have originated in the ship's exhaust, combined with that from transport from continental areas. However, no strong evidence of the ship's exhaust was found from our individual particle observations, including analyses of Fe-containing particles presented hereinafter.

3.3 Fe-containing particles: composition and morphological features implying their source

Figures 6a and 6b portray number fractions of particles containing the respective elements and mixing types with sulfate for Fe-containing particles (42 particles) observed in five samples (#01–05) affected by air masses from South Asia. Most Fe-containing particles were mixed with sulfate (Fig. 6b). Actually, S was detected from 90% of Fe-containing particles (Fig. 6a). In addition, K was found from half of the Fe-containing particles (Fig. 6a), suggesting that biomass burning affected the Fe-containing particle compositions. However, many K signals were detected from the sulfate coating. Therefore, such K implies secondary formation on Fe-containing parts rather than a source of Fe-containing parts. Both Al and Si were detected from 20% and 30% of Fe-containing particles. Very little V originating from heavy oil combustion of ships was detected from Fe-containing particles. Moreover, Na, Mg, Ca, Mn, and Zn were detected from less than 7–10% of Fe-containing particles. Both Ca and Mg can originate from biomass burning in addition to sea salt and mineral dust. Adachi et al. (2022) reported ash-bearing particles found in biomass burning smoke based on TEM analysis of fine (<2.5 μm) particles. They defined particles containing both Ca and Mg (>5 weight%) as ash-bearing particles.

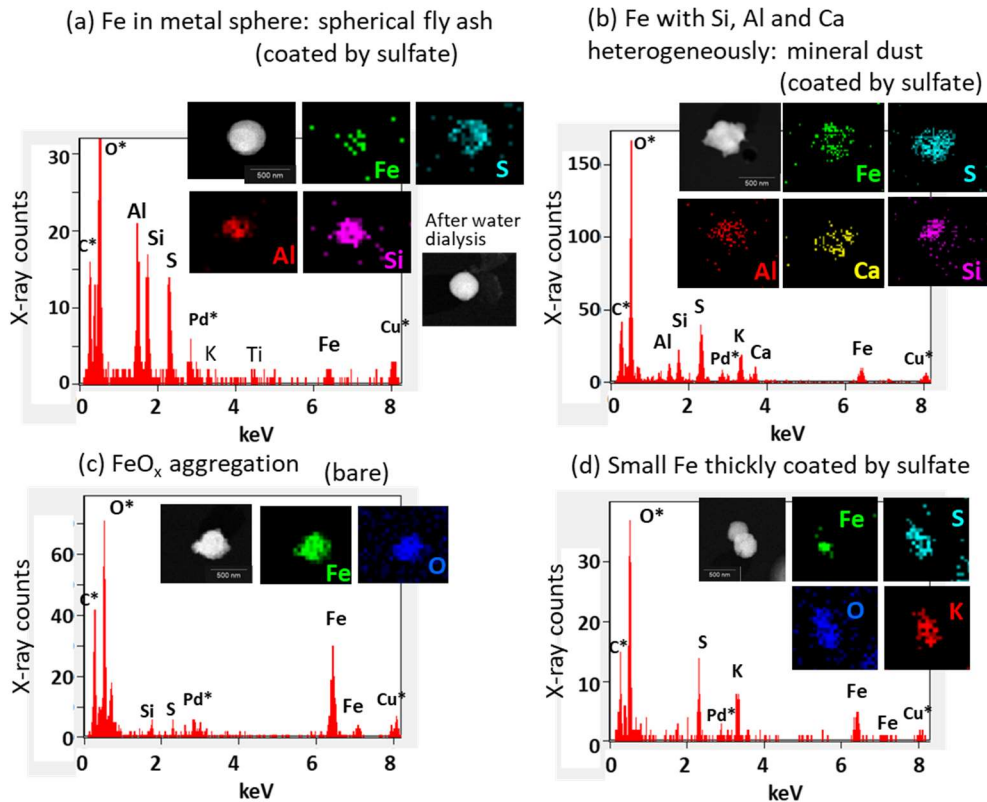
360 According to their report, ash-bearing particles from biomass burning smoke commonly exhibit aggregated shapes with complicated compositions, predominantly calcium with other elements (e.g., C, O, Mg, Al, Si, P, S, and Fe). However, for our study, the Fe-containing particles mixed with both Ca and Mg were only one (2% of Fe-containing particles). In addition, morphological features of Fe-containing particles were less like ash-bearing particles reported by Adachi et al. (2022).



365 **Figure 6: Mixing states and morphological features of Fe-containing particles of samples collected north of the equator. (a) Number fraction of each-element-containing particles in Fe-containing particles. (b) Pie chart of mixing type with sulfate. (c) Pie chart of Fe-containing part types based on constituent elements and morphology. Section 3.3 presents classification methods of Fe-containing part types. Single type in (a) is particles extracted clustered shaped particles.**

370 As shown in Figs. 4a and 4b, Fe-containing parts had some different morphological types, such as spherical or irregular shapes and homogeneous or heterogeneous mixing with other elements. Such morphological types can be related to their Fe emission source. Based on the contrast of STEM images and EDS mapping, we divided Fe-containing parts to three morphological types associated with an emission source (spherical fly ash, mineral

dust, FeO_x aggregation) and the other two types (other-shaped Fe and small Fe thickly coated by sulfate). Average ± standard deviation values of *Fe/Pd* for each type above were, respectively, 1.1±2.2, 0.18±0.14, 0.73±0.81, 1.7±0.6, and 0.07±0.05. The number fractions for the morphological types for Fe-containing particles are presented in Fig. 6c. For sample #03, the morphology after water dialysis was also referenced. In addition, examples of STEM images, the elemental map, and X-ray spectra for typical Fe-containing particles are portrayed in Fig. 7. Details of the respective morphological types are explained later in Sects. 3.3.1–3.3.4.



380

Figure 7: Examples of STEM images, elemental maps, and X-ray count spectra of typical Fe-containing particles. (a) Example of particle having a Fe-containing part in metal sphere (spherical fly ash). The metal sphere part of this particle is coated by sulfate. (b) Example of Fe-containing particle co-existing with Si, Al or Ca heterogeneously (mineral dust). The Fe, Si, Al, and Ca part of this particle is coated by sulfate. (c) Example of FeO_x aggregation particles. (d) Example of particle having small Fe-containing part thickly coated by sulfate. Asterisk (*) elements in the X-ray count spectrum represent elements contained in the background area without particles.

385

3.3.1 Fe in metal sphere (spherical fly ash)

As shown for particle A in Fig. 4 and for the particle in Fig. 7a, Fe-containing spheres with Al and/or Si were found in nine particles (21% of Fe-containing particles) from samples #03 and #04, affected by air masses from the eastern coast of India (Table S1 and Fig. 1b). In addition, Fe spheres without Al or Si were found as two particles (5% of Fe-containing particles) from sample #05, affected by air masses from the Maldives. All particles containing metal spheres of both types co-existed with sulfate. In the STEM image, such metal spheres have high contrast compared to sulfate. Such spheres remained as a residue after water dialysis. Spherical shapes of metals indicate that they were formed through evaporation at high temperatures and subsequent rapid condensation. Moreover, the shape coincides with often-encountered features of fly ash particles originating from coal combustion at power plants (e.g. Fisher et al., 1978; Yao et al., 2015; Umo et al., 2019). For this study, metal spheres composed mainly of Fe, Si or Al in our atmospheric aerosol samples are designated as spherical fly ash to distinguish them from fly ash related to emission sources that are not classified using morphology. In coal, Fe generally exists in two forms: as pyrite or aluminosilicate (Tomeczek and Palugniok, 2002). Aluminosilicate-Fe such as kaolinite and illite generally undergoes high-temperature melting and fragmentation, leading to formation as fly ash (Rathod et al., 2020). Although low-temperature combustion processes such as residential uses might not engender Fe volatilization (Flagan and Seinfeld, 2012), power plants can emit fly ash efficiently (Rathod et al., 2020). Although the mass concentration peak of fly ash emitted from power plants is super-micrometric (1–10 μm), submicrometer fly ash particles are also emitted together. They have been observed and described in the literature (Markowski and Filby, 1985; Liu et al., 2018; Umo et al., 2019).

3.3.2 Fe co-existing with Al, Si or Ca heterogeneously (mineral dust)

As shown for particle B in Fig. 4 and for the particle in Fig. 7b, some non-spherical parts containing Fe, Si, and Al were also found. Unlike the Fe-containing sphere parts explained earlier, Ca was usually detected from such non-spherical Fe-containing parts. Additionally, they have some domains of different concentrations of Fe, Al,

410 Si, and Ca. The Fe, Al, Si and Ca are main elements of silicate minerals. Mineral dust is usually composed of
some different mineral species domains (Conny, 2013; Jeong and Nousiainen, 2014; Jeong et al., 2014 and
2016; Conny et al., 2019; Ueda et al. 2020). Therefore, heterogeneous structures such as Fe, Al, Si and Ca imply
that they are mineral dusts **with no combustion-related** origin. Such Fe-containing parts regarded as mineral
dust were found in six particles (14% of Fe-containing particles) in samples #01, 03, 04, and 05 (Table S1).
415 Most particles of this type (five particles) co-existed with sulfate. Based on water dialysis of sample #03, Ca in
particle B in Fig. 4a dissolved with water dialysis, as **portrayed in Fig. 4b**. Although calcite in dust is poorly
soluble, chemical transformation from them into calcium sulfate or calcium nitrate with atmospheric aging can
alter their solubility (Okada et al., 1990, 2005; Zhang and Iwasaka, 1999; Matsuki et al. 2005).

3.3.3 FeO_x aggregation

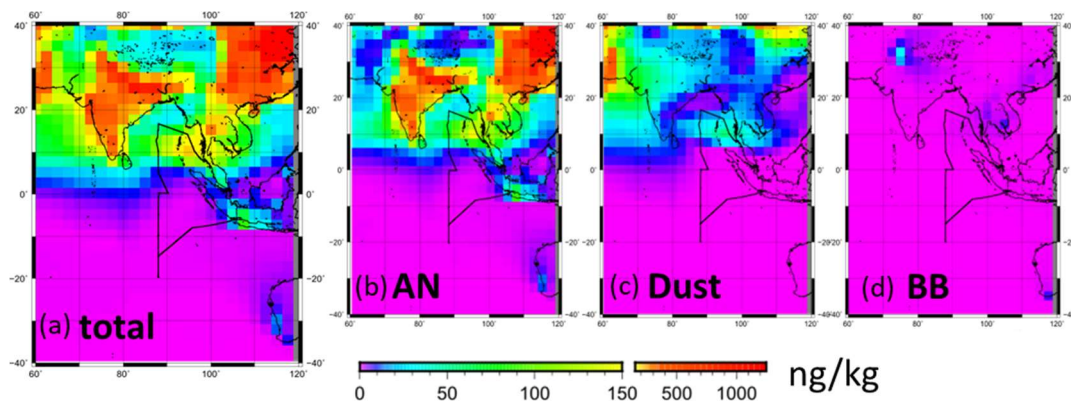
420 Some aggregate components comprising Fe and O without other metals were found as shown for a particle in
Fig. 7c. They are regarded as being FeO_x, such as magnetite and illite. Similar aggregated FeO_x nanoparticles
have often been reported from several observational studies of urban atmospheres using electron microscopy
methods (Hu et al., 2015; Adachi et al., 2016; Ohata et al., 2018), roadside environments (Sanderson et al.,
2016), and polluted remote seas (Li et al., 2017). Aggregated FeO_x co-existing with soot was also found at urban
425 sites (Ohata et al., 2018; Ueda et al., 2022). From this study, FeO_x aggregation (classified as FeO_x aggregation)
was found as without a C-rich part from three particles (7% of Fe-containing particles) in samples #02, 03, and
04, affected by air masses from India (Table S1 and Fig. 1). Two FeO_x aggregations co-existing with sulfate
were found. As explained in Sect. 3.2, soot-containing metals were also minor. The FeO_x can be emitted from
blast furnaces at Fe-working facilities (Machemer, 2004) and as exhaust from motor vehicles (Kukutschová et
430 al., 2011; Liati et al., 2015). However, considering FeO_x without soot, FeO_x aggregations examined in this study
might have originated mainly from the former source.

3.3.4 Other-shaped Fe and small Fe thickly coated by sulfate

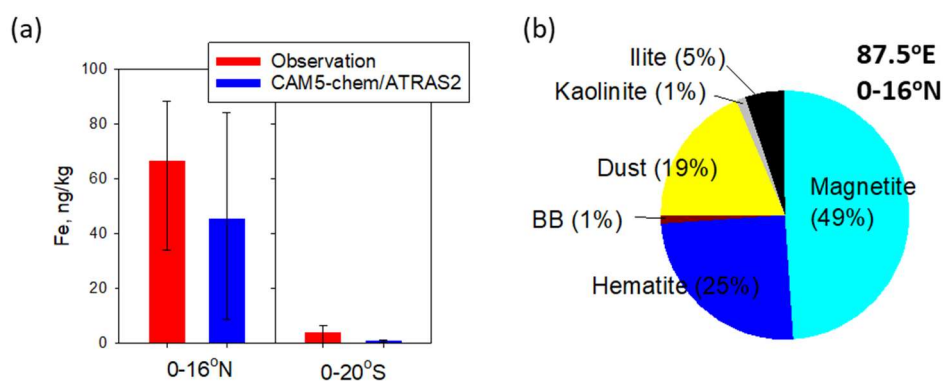
For Fe-containing parts of three particles (7% of Fe-containing particles), different shapes were found in terms of the features above: spherical fly ash, mineral dust, and FeO_x aggregation. They were classified as other-shaped Fe. **Of those**, two particles were without sulfate. For the other 19 Fe-containing particles, discriminating the shapes of Fe-containing parts was difficult because such parts were too small compared to the sulfate coating, as illustrated in Fig. 7d. Such Fe-containing particles were classified as small Fe thickly coated by sulfate separately from other shaped Fe. The number fraction was 45% of the Fe-containing particles. However, the *Fe/Pd* values (0.07 ± 0.05) from such small Fe were usually less than those of the other types.

440 3.4 Fe simulation for each source by the global model

To elucidate the origins of Fe and the model performance, Fe simulation results **obtained** using the CAM5-ATRAS model were compared with observation results. Figure 8 shows the monthly mean simulated mass concentrations in PM_{2.5} for total Fe and Fe from each source at the surface. The color scale of 0–150 ng/kg is the same as that presented for Fig. 2c. Averages of the total Fe mass concentrations for areas north and south of the equator along the ship tracks (0–16°N and 0–20°S at 87.5°E) are shown in Fig. 9a with the observed values. **The model simulations well reproduce the contrast of Fe mass between the north (high concentration) and south (low concentration) during the cruise. Although the simulated Fe mass tends to be lower than the observed Fe mass (Fig. 9a), our simulations using the recent anthropogenic Fe inventory data reported by Rathod et al. (2020) indicate higher Fe mass concentrations and show better agreement with observations than earlier estimates producing older emission inventories (Liu et al., 2022). Large uncertainties in Fe emission inventories from all sources exist, including anthropogenic sources, dust, and biomass burning origin. Moreover, different spatial and temporal scales between observation and models might influence the comparisons presented herein.**



455 **Figure 8: Spatial distribution of PM_{2.5} Fe mass concentrations simulated by the CAM5-chem/ATRAS2 model for (a) total, (b) anthropogenic (AN), (c) mineral dust (Dust), and (d) biomass burning (BB) Fe. Values are monthly averaged surface mass concentrations for November 2018.**



460 **Figure 9: PM_{2.5} Fe mass concentration simulated by CAM5-chem/ATRAS2. (a) Averaged PM_{2.5} Fe simulated value for 87.5°E and observed PM_{2.5} Fe of 87–90°E during the KH18-06 cruise. The lower and upper error bars respectively stand for the 25th and 75th percentiles. (b) Pie chart of averaged mass fraction simulated PM_{2.5} Fe for each Fe species of 0–15°N at 87.5°E. Simulated values are monthly averaged mass concentrations for November 2018.**

The CAM5-ATRAS results show that the anthropogenic Fe was dominant in PM_{2.5} Fe concentration within the area presented in Fig. 8. The averaged mass fraction of each Fe source/mineral type in the model for 0–15°N at 87.5°E estimated are depicted in Fig. 9b. The anthropogenic Fe (magnetite, hematite, illite, and kaolinite), dust Fe and biomass-burning Fe were, respectively, 80%, 19%, and 1% of the mass of PM_{2.5} Fe. Especially,

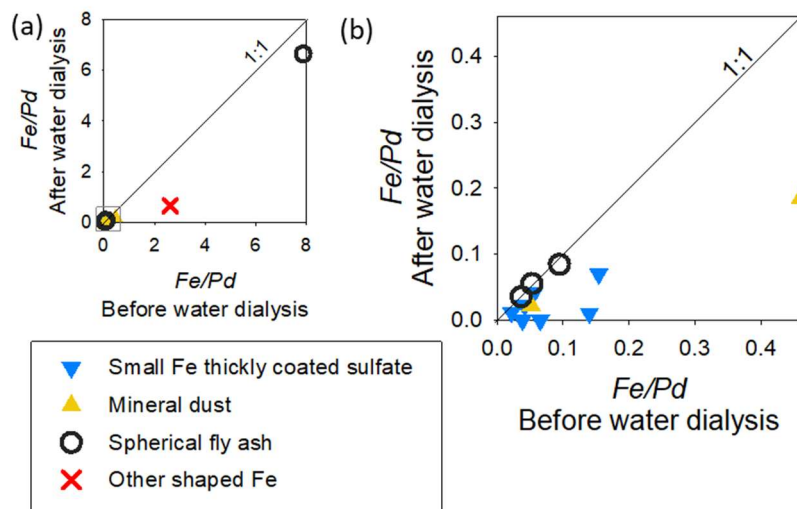
anthropogenic Fe around India has a high concentration in Fig. 8. The anthropogenic activity of the area might have affected Fe concentrations over the Indian Ocean.

The anthropogenic Fe was mostly (74% in mass of PM_{2.5} Fe) estimated as FeO_x (magnetite and hematite).
470 The mass fraction of anthropogenic aluminosilicates Fe (illite and kaolinite), which derive mainly from coal combustion, was only 6% in the model. These simulation results might underestimate the fraction of aluminosilicate Fe and overestimate the fraction of FeO_x compared to the TEM results. In the TEM samples, spherical fly ash having sufficient *Fe/Pd* values was often found (26% of Fe-containing particles) as depicted in Fig. 6. In addition, most of the fly ash particles (8 in 11 spherical fly ash particles) contained Al and/or Si.
475 Mineralogy of Fe from coal combustion in emission inventory by Rathod et al. (2020), which is used in our model, was estimated from reference to mineralogical measurements of bulk samples using Mossbauer spectrometry or from the X-ray absorption near-edge structure. Although the mineralogical transformation from fuels to by-products can be affected by the fuels and combustion temperatures, the Fe contents estimated from mineralogical measurements of coal fly ash at power plants tend to comprise both oxides (such as magnetite
480 and hematite) and clay (such as kaolinite and illite) (Hinckley et al., 1980; Szumiata et al., 2015; Waanders et al., 2003; Oakes et al., 2012; Rathod et al., 2020). However, even if Fe in spherical fly ash in our TEM samples were assumed to be composed of aluminosilicates and equivalent FeO_x, the mass fraction of aluminosilicates Fe inferred from TEM results would be larger than 13%, which is higher than our model-simulated results. The chemical composition and size-mass distribution of coal fly ash particles at the source can be affected by
485 multiple factors such as the fossil fuel composition and combustor (Markowski and Filby, 1985; Liu et al., 2018). Their lack of clarity can also affect the uncertainty of simulation for the emission of Fe originated in coal combustion and the transport according to the particle size. Such underestimation of aluminosilicates might be one factor causing the underestimation of total Fe mass concentration in our model.

3.5 Water solubility of Fe

490 **Figure 10** portrays the relation between Fe/Pd before and after water dialysis (14 particles) for sample #03. The symbols were made according to the composition and shape of residues after water dialysis. For particles containing metal sphere residues regarded as fly ash, the values of Fe/Pd after water dialysis of Figs. 10a and 10b correspond well to the values before water dialysis at a 1:1 ratio. Because Pd mass after water dialysis can be regarded as equal to that before water dialysis, such a 1:1 relation indicates the Fe in spherical fly ash as

495 almost insoluble in water. For particles aside from metal spheres containing residues, the detected values of Fe/Pd decreased, suggesting that some Fe were soluble in water. **Figure 11** portrays f_{WSFe} for Fe-containing particles on sample #03. The averages of f_{WSFe} were 48%, 6%, 58%, and 65%, respectively, for all Fe-containing particles of spherical fly ash, mineral dust, and Fe-containing particles, except spherical fly ash.



500 **Figure 10: Scatter plot of Fe weight normalized Pd weight before and after water dialysis for Fe-containing particles on sample #03. (b) is an enlarged graph of the light-gray square area of (a). Pd is a coating material in alloy for shadowing to samples.**

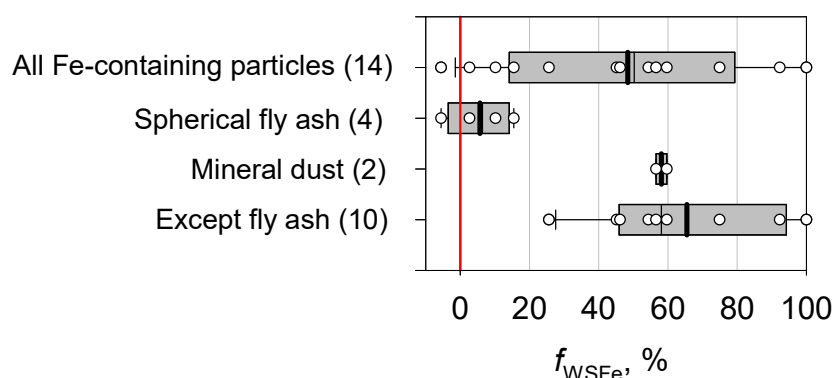


Figure 11: Box plot of the water-soluble Fe fraction (f_{WSFe}) of Fe-containing particles for sample #03. The lower boundary of the box shows the 25th percentile. The line within the box represents the median. The upper boundary of the box stands for the 75th percentile. Whiskers above and below the box respectively show the 90th and 10th percentiles. White circles show values for the respective particles.

505

Some measurement studies **examining** bulk aerosol samples have reported fractions of water-soluble Fe in all Fe (Kumar and Sarin, 2010; Baker et al., 2013; Ingall et al., 2018). After Kumar and Sarin (2010) also measured Fe in $\text{PM}_{2.5}$ at a high-altitude site in a semi-arid region of western India, they reported fractions of water-soluble Fe as 0.06–16.1%. Ingall et al. (2018) measured the water solubility of total Fe in bulk aerosol samples taken from multiple locations in the Southern and Atlantic oceans, Noida (India), Bermuda, and the eastern Mediterranean (Crete). Their fractions of water-soluble Fe were low (<5%) under samples influenced by Saharan dust, but the fractions for samples of Noida (3–20%) and samples influenced from Europe were high (17–35%), indicating an anthropogenic contribution of soluble Fe. From measurements taken of the remote ocean, Baker et al. (2013) reported Fe solubility 2.4–9.1% of aerosol collected in the Atlantic Ocean during research cruises. Compared to **the** Fe solubility **found from** the studies described above, the water-soluble Fe fraction for individual Fe-containing particles in this study tended to be estimated as higher. This finding might be attributed to the fact that our analyzed samples were smaller particles (0.3–0.8 μm samples stage diameter),

520 with a greater surface relative to the particle mass, and aged particles collected over the remote ocean, as explained below.

The values of f_{WSFe} found from this study were 20–100% in Fe-containing particles, except spherical fly ash. Among Fe-containing minerals, the fraction of water-soluble Fe in FeO_x (magnetite, goethite and hematite) and clays (such as kaolinite and illite) are very low (respectively, <0.01% and 1.5–4%), but that of ferrous and ferric sulfate is higher (50–90%) (Desboeufs et al., 2005; Journet et al., 2008; Schroth et al., 2009; Rathod et al., 2020). The Fe solubilities for many Fe-containing particles in this study were comparable to those of ferrous and ferric sulfate. Our earlier study often found non/less-sulfate-coated FeO_x in aerosol samples collected in urban Tokyo, for which we applied the same analysis (Ueda et al., 2022). However, few decreases of Fe with water dialysis were found. The difference of Fe solubility found from this urban study might be attributed to atmospheric aging processes by coating of secondary aerosol materials and Fe oxidation during transport. Some experimentation and simulation studies have indicated that Fe in minerals composed of Fe oxide and clays can be oxidized and enhanced in acidic liquid phase, such as aerosol droplets and clouds (Shi et al., 2009 and 2015; Chen et al., 2012). For the present study, most of the observed Fe-containing particles co-existing with sulfate were regarded as droplets in the atmosphere. Therefore, Fe in particles might have oxidized in liquid droplet particles in the atmosphere, after which they were later collected as water-soluble Fe, such as Fe sulfate. For Fe-containing particles in this study, the number fraction of FeO_x aggregation was less, whereas that of categorized particles to small Fe thickly coated by sulfate was higher. This result might also be affected somewhat by the loss of the water-insoluble Fe shape by change to water-soluble Fe.

All water insoluble residues in Fe-containing particles of $f_{\text{WSFe}} < 15\%$ were spherical fly ash. Although all of them co-existed with sulfate, water dialysis results indicated that the water insolubility of Fe in them was retained. Our observed insoluble sphere residues imply structural and morphological features as reasons for the insolubility of the Fe contained in aged fly ash particles. Spherical particles have the minimum surface area. In addition, the Fe is distributed in particles with other insoluble materials composed of Si and Al in the sphere.

This distribution would physically block the oxidation and dissolution of Fe. However, results of several studies
545 have suggested that Fe in similar spherical fly ash particles can dissolve in acidic particles (Chen et al., 2012;
Li et al., 2017). Li et al. (2017) observed similar submicrometer Fe-rich spheres coated by sulfate in samples
collected over the Yellow Sea affected by the East Asian continental outflow. They analyzed sulfate-rich
particles containing Fe-rich parts using nanoscale secondary ion mass spectrometry and elemental mapping with
STEM, and reported the presence of dispersed FeS⁻ (Fe sulfate) around FeO⁻ (Fe oxide)-rich part. They
550 concluded that such Fe sulfate was formed from Fe dissolution of fly ash in an acidic aqueous phase because
no other atmospheric source of Fe sulfate or process engenders its formation. Using bulk samples of coal fly
ash composed mainly of spherical particles, Chen et al. (2012) also investigated Fe dissolution. Their
experiments demonstrated that Fe in coal fly ash can dissolve in H₂SO₄ acidic aqueous solutions of pH 1 and 2.
These earlier reported study results suggest that some Fe in fly ash can exist as water-soluble Fe in sulfuric acid
555 particles. However, results of our experiments indicated that soluble Fe in spherical fly ash was considerably
less or nonexistent compared to insoluble Fe. From the present study, as shown in Sect. 3.2, sulfate particles
were found as neutralized particles, such as by ammonium. Such atmospheric conditions observed in the present
study might not have decreased pH sufficiently to enhance the Fe solubility of fly ash.

Our observation results of TEM samples suggest fly ash as an important component of fine Fe-containing
560 particles. In addition, water dialysis results suggest that Fe in aged particles over the remote ocean tend to exist
as partly or mostly water soluble, whereas Fe in spherical fly ash can maintain water-insolubility. Model
simulations have led to estimates that FeO_x was a major component in PM_{2.5} Fe of this area and that Fe from
anthropogenic aluminosilicates from sources such as coal combustion was minor. Underestimation of the mass
fraction of Fe keeping water insoluble during atmospheric transport can be a factor affecting the estimation error
565 of water-soluble Fe deposition. In addition, although Fe mineralogy is often used for the simulation of solubility
of anthropogenic Fe in percent in some models, the spherical shape of fly ash particles and the results of water
dialysis imply that Fe solubility and the change in the atmosphere depend not only on the mineralogical but also

the morphological and structural features of fly ash originating from emission processes. The presence of fly ash in fine aerosols should be noted for model simulation of water-soluble Fe and estimations based on size-segregated samples of Fe concentrations.

4 Summary and Conclusions

To elucidate the mixing states and water solubility of Fe-containing particles in remote marine areas, we conducted ship-borne aerosol observations over the Indian Ocean during the R/V Hakuho Maru cruise. After TEM samples for individual particle analysis were obtained, they were also analyzed using EDS and water dialysis. Most of the particles were composed mainly of sulfate neutralized by ammonium or potassium: the particle number fraction, 0.6–3.0%, of particles on a sample stage of 0.3–0.8 μm diameter contained Fe. They mostly co-existed with sulfate.

Backward air mass trajectory analyses suggest that air masses south of the equator were transported from southern India. Both the correlations of the respective elements measured using chemical analysis for bulk $\text{PM}_{2.5}$ samples and the absence of V and soot for individual Fe-containing particles implied that the Fe in particles was transported mainly from around the continent rather than from ship exhaust. The Fe in particles was found to be 26% metal spheres, often co-existing with Al or Si, regarded as fly ash, 14% as irregularly shaped heterogeneously co-existing with Si, Al or Ca, regarded as mineral dust, and 7% as FeO_x aggregations.

Global model simulations using a recent emissions inventory mostly reproduced the observed $\text{PM}_{2.5}$ Fe concentrations in the north and south during the cruise. The model simulations suggested that $\text{PM}_{2.5}$ Fe over the observation site was influenced strongly by anthropogenic Fe emissions around India. In contrast, compared with the morphological features of observed Fe, the simulations tend to overestimate the fractions of anthropogenic FeO_x and to underestimate the fraction of Fe in aluminosilicates originating from coal combustion.

Water-dialysis analysis for a TEM sample indicated that about half of the Fe in Fe-containing particles was soluble in water. However, Fe in spherical fly ash particles was almost insoluble in water, even when co-existing with sulfate. Dissolution and oxidation of Fe in spherical fly ash might have been blocked by the small surface of the sphere and the structure of Fe-dispersion in other insoluble aluminosilicates.

595 Our results obtained from shipboard observations and individual fine aerosol analysis indicate that Fe of various types, such as fly ash, FeO_x, and mineral dust, coexist with sulfate over the remote Indian Ocean, and indicate that their solubilities differ among types. Although the model simulations show good agreement with the observed Fe mass concentrations, we also find a marked difference in the mass fractions of mineral sources of model simulations compared to the observed Fe types. Earlier studies have indicated that anthropogenic fine
600 Fe tends to be composed mainly of FeO_x, with increased solubility occurring along with aging. However, our results suggest that Fe in spherical fly ash can stand out in fine aerosols over the remote ocean and maintain water insolubility. For accurate estimation of the effects of atmospheric Fe on marine biogeochemical activity, more proper attention must be devoted to morphological and mineral types of Fe depending on the source, and especially to insoluble Fe in fly ash.

605

Acknowledgments

We are indebted to staff members of the Hakuho Maru for assisting our work on board and to Prof. K. Osada of Nagoya University for support and technical advice. We also extend our gratitude for technical support from the High Voltage Electron Microscope Laboratory of Nagoya University. We gratefully acknowledge the
610 NOAA Air Resources Laboratory (ARL) for providing the HYSPLIT transport model (<http://www.arl.noaa.gov/ready.html>). This study was supported by Ministry of Education, Culture, Sports, Science, and Technology and the Japan Society for the Promotion of Science (MEXT/JSPS) KAKENHI Grants 18H03369, 18J40204, 19K20438, 22K18023, JP19H04253, JP19H05699, JP19KK0265, JP20H00196,

JP20H00638, JP21K12230, JP22H03722, and JP22F22092, MEXT Arctic Challenge for Sustainability phase
615 II (ArCS-II; JPMXD1420318865) projects, and the Environment Research and Technology Development Fund
2–2003 (JPMEERF20202003) of the Environmental Restoration and Conservation Agency. M.L. acknowledges
the support of JSPS Postdoctoral Fellowships for Research in Japan (Standard).

Data availability

Back-trajectory data were calculated from the NOAA HYSPLIT model
620 (<https://www.ready.noaa.gov/HYSPLIT.php>, last access: 08 March 2018). Other data will be provided upon
request.

Author contributions

SU, YI and FT designed the study. SU analyzed TEM samples and wrote the paper. YI worked on board for
aerosol sampling and measurement. YI and FT contributed to chemical analyses of PM_{2.5} samples. HM and ML
625 conducted numerical model simulations using CAM5-ATRAS.

Competing interests

The authors declare that they have no conflict of interest.

References

Adachi, K., Moteki, N., Kondo, Y. and Igarashi, Y.: Mixing states of light-absorbing particles measured using
630 a transmission electron microscope and a single-particle soot photometer in Tokyo, Japan, *J. Geophys. Res.*
Atmos., 121, 9153–9164, doi:10.1002/2016JD025153, 2016.

- Andreae, M. O.: Soot carbon and excess fine potassium: long-range transport of combustion-derived aerosols, *Science*, 220, 11481151, doi: 10.1126/science.220.4602.1148, 1983.
- Baker, A. R., Adams, C., Bell, T. G., Jickells, T. D., and Ganzeveld, L.: Estimation of atmospheric nutrient
635 inputs to the Atlantic Ocean from 50°N to 50°S based on large-scale field sampling: Iron and other dust-associated elements, *Global Biogeochem. Cycles*, 27, 755–767, doi:10.1002/gbc.20062, 2013.
- Bray, C. D., Battye, W. H. and Aneja, V. P.: The role of biomass burning agricultural emissions in the Indo-Gangetic Plains on the air quality in New Delhi, India, *Atmos. Environ.*, 218, 116983, doi:10.1016/j.atmosenv.2019.116983, 2019.
- 640 Bigg, E. K.: Comparison of aerosol at four baseline atmospheric monitoring stations, *J. Appl. Meteorol.*, 19, 521–533, doi:10.1175/1520-0450(1980)019<0521:COAAFB>2.0.CO;2., 1980.
- Bradley, W. F. and Grim, R. E.: High temperature thermal effects of clay and related materials, *American Mineralogist, Journal of Earth and Planetary Materials*, 36(3–4), 182–201, 1951.
- Chen, H., Laskin, A., Baltrusaitis, J., Gorski, C. A., Scherer, M. M., and Grassian, V. H.: Coal fly ash as a
645 source of iron in atmospheric dust, *Environ. Sci. Technol.*, 46, 2112–2120, doi:10.1021/Es204102f, 2012.
- Chen, Y. Wild, O., Conibear, L., Ran, L., He, J. Wang, L., and Wang, Y.: Local characteristics of and exposure to fine particulate matter (PM_{2.5}) in four Indian megacities, *Atmos. Environ.*, X5, 100052, doi:10.1016/j.aeaoa.2019.100052, 2020.
- Chuang, P. Y., Duvall, R. M., Shafer, M. M., and Schauer, J. J.: The origin of water soluble particulate iron in
650 the Asian atmospheric outflow, *Geophys. Res. Lett.*, 32, L07813, doi: 10.1029/2004GL021946, 2005.
- Conny, J. M.: Internal composition of atmospheric dust particles from focused ion-beam scanning electron microscopy, *Environ. Sci. Technol.*, 47, 8575–8581, doi:org/10.1021/es400727x, 2013.
- Conny, J. M., Willis, R. D., and Ortiz-Montalvo, D. L.: Analysis and optical modeling of individual heterogeneous Asian Dust Particles collected at Mauna Loa Observatory, *J. Geophys. Res. – Atmos.*, 124(5),
655 270–2723, doi:10.1029/2018JD029387, 2019.

- Corbin, J. C., Mensah, A. A., Pieber, S. M., Orasche, J., Michalke, B., Zanatta, M., Czech, H., Massabò, D., Buatier de Mongeot, F., Mennucci, C., El Haddad, I., Kumar, N. K., Stengel, B., Huang, Y., Zimmermann, R., Prévôt, A. S. H., and Gysel, M.: Trace metals in soot and PM_{2.5} from heavy-fuel-oil combustion in a marine engine, *Environ. Sci. Technol.*, 52 (11), 6714–6722, doi: 10.1021/acs.est.8b01764, 2018.
- 660 Cwiertny, D. M., Baltrusaitis, J., Hunter, G. J., Laskin, A., Scherer, M. M., and Grassian, V. H.: Characterization and acid-mobilization study of iron-containing mineral dust source materials, *J. Geophys. Res. Atmos.*, 113(D5), doi:10.1029/2007JD009332, 2008.
- de Baar, H. J. W., Boyd, P. W., Coale, K. H., Landry, M. R., Tsuda, A., Assmy, P., Bakker, D. C. E., Bozec, Y., Barber, R. T., Brzezinski, M. A., Buesseler, K. O., Boye, M., Hiscock, W. T., Laan, P., Lancelot, C., Law, C.S., Lvasseur, M., Marchetti, A., Millero, F. J., Nishioka, J., Nojiri, Y., Oijen, T., Riebesell, U., Rijkenberg, M. J. A., Saito, H., Takeda, S., Timmermans, K. R., Veldhuis, M. J. W., Waite, A. M., and Wong, C.: Synthesis of iron fertilization experiments: from the Iron Age in the Age of Enlightenment, *Journal of Geophysical Research*, 110, p. C09S16, doi:10.1029/2004JC002601, 2005.
- 670 Desboeufs, K. V., Sofikitis, A., Losno, R., Colin, J. L., and Ausset, P.: Dissolution and solubility of trace metals from natural and anthropogenic aerosol particulate matter, *Chemosphere*, 58(2), 195–203, doi:10.1016/j.chemosphere.2004.02.025, 2005.
- Duce, R. A. and Tindale, N. W.: Atmospheric transport of iron and its deposition in the ocean, *Limnol. Oceanogr.*, 36, 1715–1726, doi: 10.4319/lo.1991.36.8.1715, 1991.
- 675 Ferek, R. J., Lazrus, A. L., and Winchester, J. W.: Electron microscopy of acidic aerosols collected over the northeastern United States, *Atmos. Environ.*, 17, 1545–1561, doi:10.1016/0004-6981(83)90308-6, 1983.
- Fisher, G. L., Prentice, B. A., Silberman, D., Ondov, J. M., Biermann, A. H., Ragaini, R. C., and McFarland, A. R.: Physical and morphological studies of size-classified coal fly ash, *Environ. Sci. Technol.*, 12, 447–451, doi:10.1021/es60140a008, 1978.

- 680 Flagan, R. C. and Seinfeld, J. H.: Fundamentals of air pollution engineering. Courier Corporation, 2012.
- Frank, E. R. and Lodge, J. P.: Morphological identification of airborne particles with the electron microscope, *J. Microscope*, 6, 449–456, 1967.
- Gras, J. L. and Ayers, G. P.: On sizing impacted sulfuric acid aerosol particles, *J. Appl. Meteorol.*, 18, 634–638, doi:10.1175/1520-0450(1979)018<0634:OSISAA>2.0.CO;2, 1979.
- 685 Guieu, C., Bonnet, S., Wagener, T., and Loÿe-Pilot, M.-D.: Biomass burning as a source of dissolved iron to the open ocean? *Geophys. Res. Lett.*, 32, L19608, doi: 0.1029/2005GL022962, 2005.
- Guttikunda, S. K., Goel, R., and Pant, P.: Nature of air pollution, emission sources, and management in the Indian cities, *Atmos. Environ.*, 95, 501–510, doi: 10.1016/j.atmosenv.2014.07.006, 2014.
- Harrison, P. J., Boyd, P. W., Varela, D. E., Takeda, S., Shiimoto, A., and Odate, T.: Comparison of factors
690 controlling phytoplankton productivity in the NE and NW subarctic Pacific gyres, *Prog. Oceanogr.*, 43, 205–234, doi:10.1016/S0079-6611(99)00015-4, 1999.
- Hidemori, T., Nakayama, T., Matsumi, Y., Kinugawa, T., Yabushita, A., Ohashi, M., Miyoshi, T., Irei, S., Takami, A., Kaneyasu, N., Yoshino, A., Suzuki, R., Yumoto, Y., and Hatakeyama, S.: Characteristics of atmospheric aerosols containing heavy metals measured on Fukue Island, Japan, *Atmos. Environ.*, 97, 447–
695 455, doi:10.1016/j.atmosenv.2014.05.008, 2014.
- Hinckley, C. C., Smith, G. V., Twardowska, H., Saporoschenko, M., Shiley, R. H., and Griffen, R. A.: Mössbauer studies of iron in Lurgi gasification ashes and power plant fly and bottom ash, *Fuel*, 59(3), 161–165. [https://doi.org/10.1016/0016-2361\(80\)90160-X](https://doi.org/10.1016/0016-2361(80)90160-X), 1980.
- Hu, Y., Lin, J., Zhang, S., Kong, L., Fu, H., and Chen, J.: Identification of the typical metal particles among
700 haze, fog, and clear episodes in the Beijing atmosphere, *Sci. Total Environ.*, 511, 369–380, doi: 10.1016/j.scitotenv.2014.12.071, 2015.

- Ingall, E. D., Feng, Y., Longo, A. F., Lai, B., Shelley, R. U., Landing, W. M., Morton, P. L., Nenes, A., Mihalopoulos, N., Violaki, K., Gao, Y., Sahai, S., and Castorina, E.: Enhanced iron solubility at low pH in global aerosols, *Atmosphere*, 9, 201, doi:10.3390/atmos9050201, 2018.
- 705 Ito, A.: Atmospheric processing of combustion aerosols as a source of bioavailable iron, *Environ. Sci. Technol. Lett.*, 2, 70–75, doi: 10.1021/acs.estlett.5b00007, 2015
- Ito, A. and Feng, Y.: Role of dust alkalinity in acid mobilization of iron, *Atmos. Chem. Phys.*, 10, 9237–9250, doi:10.5194/acp-10-9237-2010, 2010.
- Iwamoto, Y., Narita, Y., Tsuda, A., and Uematsu, M.: Single particle analysis of oceanic suspended matter
710 during the SEEDS II iron fertilization experiment, *Marine Chemistry*, 113, 212–218, doi: 10.1016/j.marchem.2009.02.002, 2009.
- Iwamoto, Y., Yumimoto, K., Toratani, M., Tsuda, A., Miura, K., Uno, I., and Uematsu, M.: Biogeochemical implications of increased mineral particle concentrations in surface waters of the northwestern North Pacific during an Asian dust event, *Geophys. Res. Lett.*, 38, L01604, doi:10.1029/2010GL045906, 2011.
- 715 Jeong, G. Y., Kim, J. Y., Seo, J., Kim, G. M., Jin, H. C., and Chun, Y.: Long-range transport of giant particles in Asian dust identified by physical, mineralogical, and meteorological analysis, *Atmos. Chem. Phys.*, 14, 505–521, doi:10.5194/acp-14-505-2014, 2014.
- Jeong, G. Y. and Nousiainen, T.: TEM analysis of the internal structures and mineralogy of Asian dust particles and the implications for optical modeling, *Atmos. Chem. Phys.*, 14, 7233–7254, doi:10.5194/acp-14-7233-
720 2014, 2014.
- Jeong, G. Y., Park, M. Y., Kandler, K., Nousiainen, T., and Kemppinen, O.: Mineralogical properties and internal structures of individual fine particles of Saharan dust, *Atmos. Chem. Phys.*, 16, 12397–12410, doi:10.5194/acp-16-12397-2016, 2016.

- Jickells, T. D. An, Z. S. Andersena, K. K., Baker, A. R., Bergamettin, G. Brooks, N., Cao, J. J., Boyd, P. W.,
725 DUCE, R. A., and Torres, R.: Global iron connections between desert dust, ocean biogeochemistry, and
climate, *Science*, 308, 67–71, doi: 10.1126/science.1105959, 2005.
- Journet, E., Desboeufs, K. V., Caquineau, S., and Colin, J. L.: Mineralogy as a critical factor of dust iron
solubility, *Geophys. Res. Lett.*, 35(L07805), doi:10.1029/2007GL031589, 2008.
- Kanawade, V. P., Srivastava, A. K., Ram, K., Asmi, E., Vakkari, V., Soni, V. K., Varaprasad, V., and Sarangi,
730 C.: What caused severe air pollution episode of November 2016 in New Delhi? *Atmos. Environ.*, 222,
117125, doi: 10.1016/j.atmosenv.2019.117125, 2020.
- Kawamura, K. and Kaplan, I. R.: Motor exhaust emissions as a primary source for diocarboxylic acids in Los
Angeles ambient air, *Environ Sci. Technol.*, 21, 105–110, doi:10.1021/es00155a014, 1987.
- Kompalli, S. K., Babu, S. N. S., Moorthy, K. K., Satheesh, S. K., Gogoi, M. M., Nair, V. S., Jayachandran, V.
735 N., Liu, D., Flynn, M. J., and Coe, H.: Mixing state of refractory black carbon aerosol in the South Asian
outflow over the northern Indian Ocean during winter, *Atmos. Chem. Phys.*, 21, 9173–9199, 2, doi:
10.5194/acp-21-9173-2021, 2021.
- Kukutschová, J., Moravec, P., Tomášek, V., Matějka, V., Smolík, J., Schwarz, J., Seidlerová, J., Safářová, K.,
and Filip, P.: On airborne nano/micro-sized wear particles released from low-metallic automotive brakes,
740 *Environ. Pollut.*, 159(4), 998–1006, doi:10.1016/j.envpol.2010.11.036, 2011.
- Kumar, A. and Sarin, M.: Aerosol iron solubility in a semi-arid region: Temporal trend and impact of
anthropogenic sources, *Tellus Ser. B Chem. Phys. Meteorol.*, 62, 125–132, doi: 10.1111/j.1600-
0889.2009.00448.x, 2010.
- Li, W., Xu, L., Liu, X., Zhang, J., Lin, Y., Yao, X., Gao, H., Zhang, D., Chen, J., Wang, W., Harrison, R. M.,
745 Zhang, X., Shao, L., Fu, P., Nenes, A., and Shi, Z.: Air pollution – aerosol interactions produce more
bioavailable iron for ocean ecosystems, *Sci. Adv.* 3, e1601749, doi:10.1126/sciadv.1601749, 2017.

- Liati, A., Pandurangi, S. S., Boulouchos, K., Schreiber, D., and Dasilva, Y. A. R.: Metal nanoparticles in diesel exhaust derived by in-cylinder melting of detached engine fragments, *Atmos. Environ.*, 101, 34–40, doi:10.1016/j.atmosenv.2014.11.014, 2015.
- 750 Liu, M. and Matsui, H.: Aerosol radiative forcings induced by substantial changes in anthropogenic emissions in China from 2008 to 2016, *Atmos. Chem. Phys.*, 21, 5965–5982, doi:10.5194/acp-21-5965-2021, 2021a.
- Liu, M. and Matsui, H.: Improved simulations of global black carbon distributions by modifying wet scavenging processes in convective and mixed-phase clouds, *J. Geophys. Res. – Atmos.*, 126, e2020JD033890, doi:10.1029/2020JD033890, 2021b.
- 755 Liu, M., Matsui, H., Hamilton, D., Lamb, K. D., Rathod, S. D., Schwarz, J. P., and Mahowald, N. M.: The underappreciated role of anthropogenic sources in atmospheric soluble iron flux to the Southern Ocean, *npj Clim. Atmos. Sci.*, 5, 28, doi: 10.1038/s41612-022-00250-w, 2022.
- Liu, H., Wang, Y., and Wendt, J. O.: Particle size distributions of fly ash arising from vaporized components of coal combustion: A comparison of theory and experiment, *Energy Fuels*, 32(4), 4300–4307, doi: 760 10.1021/acs.energyfuels.7b03126, 2018.
- Luo, C., Mahowald, N., Bond, T., Chuang, P. Y., Artaxo, P., Siefert, R., Chen, Y., and Schauer, J.: Combustion iron distribution and deposition, *Glob. Biogeochem. Cycles*, 22, GB1012, doi: 10.1029/2007GB002964, 2008.
- Machemer, S. D.: Characterization of airborne and bulk particulate from iron and steel manufacturing facilities, 765 *Environ. Sci. Technol.*, 38(2), 381–389, doi:10.1021/es020897v, 2004.
- Mahowald, N. M., Baker, A. R., Bergametti, G., Brooks, N., Duce, R. A., Jickells, T. D., Kubilay, N., Prospero, J. M., and Tegen, I.: Atmospheric global dust cycle and iron inputs to the ocean, *Glob. Biogeochem. Cycles*, 19, GB402, 2005.
- Mahowald, N. M., Engelstaedter, S., Luo, C., Sealy, A., Artaxo, P., Benitez-Nelson, C., Bonnet, S., Chen, Y., 770 Chuang, P. Y., Cohen, D. D., Dulac, F., Herut, B., Johansen, A. M., Kubilay, N., Losno, R., Maenhaut, W.,

- Paytan, A., Prospero, J. M., Shank, L. M., and Siefert R. L.: Atmospheric Iron Deposition: Global Distribution, Variability, and Human Perturbations, *Annu. Rev. Marine. Sci.*, 1, 245–278, doi:10.1146/annurev.marine.010908.163727, 2009.
- 775 Mahowald, N. M., Hamilton, D. S., Mackey, K. R. M., Moore, J. K., Baker, A. R., Scanza, R. A., and Zhang, Y.: Aerosol trace metal leaching and impacts on marine microorganisms, *Nature Communications*, 9(1), doi:10.1038/s41467-018-04970-7, 2018.
- Markowski, G. R. and Filby, R.: Trace Element Concentration as a Function of Particle Size in Fly Ash from a Pulverized Coal Utility Boiler, *Environ. Sci. Technol.*, 19, 796–804, doi:10.1021/es00139a005, 1985.
- Martin, J. H. and Fitzwater, S.: Iron deficiency limits phytoplankton growth in the north-east Pacific subarctic, 780 *Nature*, 331, 947–975, 1988.
- Matsui, H.: Development of a global aerosol model using a two-dimensional sectional method: 1. Model design, *J. Adv. Model. Earth Syst.*, 9, 1921–1947, doi:10.1002/2017ms000936, 2017.
- Matsui, H.: Black carbon absorption efficiency under preindustrial and present-day conditions simulated by a size- and mixing-state-resolved global aerosol model, *J. Geophys. Res. – Atmos*, 125, e2019JD032316, 785 doi:10.1029/2019 JD032316, 2020.
- Matsui, H. and Mahowald, N.: Development of a global aerosol model using a two-dimensional sectional method: 2. Evaluation and sensitivity simulations, *J. Adv. Model. Earth Syst.*, 9, 1887–1920, doi:10.1002/2017ms000937, 2017.
- Matsui, H., Koike, M., Kondo, Y., Fast, J. D., and Takigawa, M.: Development of an aerosol microphysical 790 module: Aerosol Two-dimensional bin module for foRmation and Aging Simulation (ATRAS), *Atmos. Chem. Phys.*, 14, 10315–10331, doi:10.5194/acp-14-10315-2014, 2014.
- Matsui, H., Hamilton, D. S., and Mahowald, N. M.: Black carbon radiative effects highly sensitive to emitted particle size when resolving mixing-state diversity, *Nat. Commun.*, 9, 3446, doi:10.1038/s41467-018-05635-1, 2018a.

- 795 Matsui, H., Mahowald, N. M., Moteki, N., Hamilton, D. S., Ohata, S., Yoshida, A., Koike, M., Scanza, R. A.,
and Flanner, M. G.: Anthropogenic combustion iron as a complex climate forcer, *Nat. Commun.*, 9, 1593,
doi:10.1038/s41467-018-03997-0, 2018b.
- Matsuki, A., Iwasaka, Y., Shi, G., Zhang, D., Trochkin, D., Yamada, M., Kim, Y.-S., Chen, B., Nagatani, T.,
Miyazawa, T., Nagatani, M., and Nakata, H.: Morphological and chemical modification of mineral dust:
800 Observational insight into the heterogeneous uptake of acidic gases, *Geophys. Res. Lett.*, 32, L22806,
doi:10.1029/2005GL024176, 2005.
- Miki, Y., Ueda, S., Miura, K., Furutani, H., and Uematsu, M.: Atmospheric Fe-containing particles over the
North Pacific Ocean: The mixing states with water soluble materials, *Earozoru Kenkyu*, 29, 104–111, 2014.
- Mossop, S. C.: Stratospheric particles at 20 km, *Nature*, 199, 325–326, doi:10.1016/0016-7037(65)90017-7,
805 1963.
- Moteki, N., Adachi, K., Ohata, S., Yoshida, A., Harigaya, T., Koike, M., and Kondo, Y.: Anthropogenic iron
oxide aerosols enhance atmospheric heating, *Nat. Commun.*, 8, 15329, doi: 10.1038/ncomms15329, 2017.
- Murr, L. E. and Soto, K. F.: A TEM study of soot, carbon nanotubes, and related fullerene nanopholyhedra in
common fuel–gas combustion sources, *Mater. Charact.*, 55, 50–65. 2005.
- 810 Myriokefalitakis, S., Ito, A., Kanakidou, M., Nenes, A., Krol, M. C., Mahowald, N. M., Scanza, R. A., Hamilton,
D. S., Johnson, M. S., Meskhidze, N., Kok, J. F., Guieu, C., Baker, A. R., Jickells, T. D., Sarin, M. M.,
Bikkina, S., Shelley, R., Bowie, A., Perron, M. M. G., and Duce, R. A.: Reviews and syntheses: the
GESAMP atmospheric iron deposition model intercomparison study, *Biogeosciences*, 15, 6659–6684,
<https://doi.org/10.5194/bg-15-6659-2018>, 2018.
- 815 Narukawa, M., Kawamura, K., Takeuchi, N., and Nakajima, T.: Distribution of dicarboxylic acids and carbon
isotopic compositions in aerosols from 1997 Indonesian forest fires, *Geophys. Res. Lett.*, 26, 3101–3104,
doi: 10.1029/1999GL010810, 1999.

- Oakes, M., Ingall, E. D., Lai, B., Shafer, M. M., Hays, M. D., and Liu, Z. G.: Iron solubility related to particle sulfur content in source emission and ambient fine particles, *Environmental Science and Technology*, 46(12), 6637–6644, doi:10.1021/es300701c, 2012.
- 820
- Ohata, S., Yoshida, A., Moteki, N., Adachi, K., Takahashi, Y., Kurisu, M., and Koike, M.: Abundance of light-absorbing anthropogenic iron oxide aerosols in the urban atmosphere and their emission sources, *J. Geophys. Res. Atmos.*, 123, 8115–8134, doi:10.1029/2018 JD028363, 2018.
- Ojha, N., Sharma, A., Kumar, M., Girach, I., Ansari, T. U., Sharma, S. K., Singh, N., Pozzer, A., and Gunthe, S. S.: On the widespread enhancement in fine particulate matter across the Indo-Gangetic Plain towards winter, *Sci. Rep.*, 10, 5862, 5862 doi:10.1038/s41598-020-62710-8, 2020.
- 825
- Okada, K.: Nature of individual hygroscopic particles in the urban atmosphere, *J. Meteor. Soc. Japan*, 61, 727–735, 1983.
- Okada, K. and Hitzenberger, R. M.: Mixing properties of individual submicrometer aerosol particles in Vienna, *Atmos. Environ.*, 35, 5617–5628, doi:10.1016/S1352-2310(01)00126-1, 2001.
- 830
- Okada, K., Naruse, H., Tanaka, T., Nemoto, O., Iwasaka, Y., Wu, P.-M., Ono, A., Duce, R. A., Uematsu, M., Merrill, J. T., and Arao, K.: X-ray spectrometry of individual Asian dust-storm particles over the Japanese islands and the North Pacific Ocean, *Atmos. Environ.*, 24A, 1369–1378, doi: 10.1016/0960-1686(90)90043-M, 1990.
- 835
- Okada, K., Qin, Y., and Kai, K.: Elemental composition and mixing properties of atmospheric mineral particles collected in Hohhot, China, *Atmos. Res.*, 73, 45–67, doi: 10.1016/j.atmosres.2004.08.001, 2005.
- Rathod, S. D., Hamilton, D. S., Mahowald, N. M., Klimont, Z., Corbett, J. J., and Bond, T. C.: A mineralogy-based anthropogenic combustion-iron emission inventory, *J. Geophys. Res. – Atmos.*, 125, e2019JD032114. doi:10.1029/2019JD032114, 2020.
- 840
- Rolph, G., Stein, A., and Stunder, B.: Real-time Environmental Applications and Display sYstem: READY, *Environ. Modell. Softw.*, 95, 210–228, doi:10.1016/j.envsoft.2017.06.025, 2017.

- Sakata, K., Kurisu, M., Takeichi, Y., Sakaguchi, A., Tanimoto, H., Tamenori, Y., Matsuki, A., and Takahashi, Y.: Iron (Fe) speciation in size-fractionated aerosol particles in the Pacific Ocean: The role of organic complexation of Fe with humic-like substances in controlling Fe solubility, *Atmos. Chem. Phys.*, 22, 9461–9482, <https://doi.org/10.5194/acp-22-9461-2022>, 2022.
- 845
- Sanderson, P., Su, S. S., Chang, I. T. H., Delgado Saborit, J. M., Kepaptsoglou, D. M., Weber, R. J. M., and Harrison, R. M.: Characterisation of iron-rich atmospheric submicrometre particles in the roadside environment, *Atmos. Environ.*, 140, 167–175, doi:10.1016/j.atmosenv.2016.05.040, 2016.
- Scanza, R. A., Hamilton, D. S., Perez Garcia-Pando, C., Buck, C., Baker, A., and Mahowald, N. M.: Atmospheric processing of iron in mineral and combustion aerosols: development of an intermediate-complexity mechanism suitable for Earth system models, *Atmos. Chem. Phys.*, 18, 14175–14196, <https://doi.org/10.5194/acp-18-14175-2018>, 2018.
- 850
- Schroth, A. W., Crusius, J., Sholkovitz, E. R., and Bostick, B. C.: Iron solubility driven by speciation in dust sources to the ocean, *Nature Geoscience*, 2(5), 337–340, doi:10.1038/ngeo501, 2009.
- 855
- Sedwick, P. N., Sholkovitz, E. R., and Church, T. M.: Impact of anthropogenic combustion emissions on the fractional solubility of aerosol iron: Evidence from the Sargasso Sea, *Geochem. Geophys. Geosyst.*, 8, Q10Q06, doi: 10.1029/2007GC001586, 2007.
- Shi, Z., Krom, M. D., Bonneville, S., Baker, A. R., Jickells, T. D., and Benning, L. G.: Formation of iron nanoparticles and increase in iron reactivity in mineral dust during simulated cloud processing, *Environ. Sci. Technol.*, 43, 6592–6596, 2009.
- 860
- Shi, Z., Krom, M. D., Bonneville, S., and Benning, L. G.: Atmospheric processing outside clouds increases soluble iron in mineral dust, *Environ. Sci. Technol.*, 49, 1472–1477, 2015.
- Shi, Z., Krom, M. D., Jickells, T. D., Bonneville, S., Carslaw, K. S., Mihalopoulos, N., Baker, A. R., and Benning, L. G.: Impacts on iron solubility in the mineral dust by processes in the source region and the atmosphere: a review, *Aeolian Res.*, 5, 21–42, doi: 10.1016/j.aeolia.2012.03.001, 2012.
- 865

Shaik, D. S., Kant, Y., Mitra, D., Singh, A., Chandola, H. C., Sateesh, M., Babu, S. S., and Chauhan, P.: Impact of biomass burning on regional aerosol optical properties: A case study over northern India, *J. Environ. Manage.*, 244, 328–343, doi:10.1016/j.jenvman.2019.04.025, 2019.

870 Stein, A. F., Draxler, R. R., Rolph, G. D., Stunder, B. J. B., Cohen, M. D., and Ngan, F.: NOAA's HYSPLIT atmospheric transport and dispersion modeling system, *B. Am. Meteorol. Soc.*, 96, 2059–2077, doi:10.1175/BAMS-D-14-00110.1, 2015.

Szumiata, T., Gzik-Szumiata, M., Brzózka, K., Górka, B., Gawroński, M., Świetlik, R., and Trojanowska, M.: Iron-containing phases in fly ashes from different combustion systems, *Nukleonika*, 60(1), 151–154, doi:10.1515/nuka-2015-0030, 2015.

875 Takahashi, Y., Furukawa, T., Kanai, Y., Uematsu, M., Zheng, G., and Marcus, M. A.: Seasonal changes in Fe species and soluble Fe concentration in the atmosphere in the Northwest Pacific region based on the analysis of aerosols collected in Tsukuba, Japan, *Atmos. Chem. Phys.*, 13, 7695–7710, <https://doi.org/10.5194/acp-13-7695-2013>, 2013.

880 Takigawa, M., Patra, P. K., Matsumi, Y., Dhaka, S. K., Nakayama, T., Yamaji, K., Kajino, M., and Hayashida, S.: Can Delhi's pollution be affected by crop fires in the Punjab Region? *SOLA*, 16, 86–91, doi:10.2151/sola.2020-015, 2020.

Tomeczek, J. and Palugniok, H.: Kinetics of mineral matter transformation during coal combustion, *Fuel*, 81(10), 1251–1258. doi: 10.1016/S0016-2361(02)00027-3, 2002

885 Tsuda, A., Takeda, S., Saito, H., Nishioka, J., Kudo, I., Nojiri, Y., Suzuki, K., Uematsu, M., Wells, M. L., Tsumune, D., Yoshimura, Y., Aono, T., Aramaki, T., Cochlan, W. P., Hayakawa, M., Imai, K., Isada, T., Iwamoto, Y., Johnson, W. K., Kameyama, S., Kato, S., Kiyosawa, H., Kondo, Y., Levasseur, M., Machida, R. J., Nagao, I., Nakagawa, F., Nakanishi, T., Nakatsuka, S., Narita, A., Noiri, Y., Obata, H., Ogawa, H., Oguma, K., Ono, T., Sakuragi, T., Sasakawa, M., Sato, M., Shimamoto, A., Takata, H., Trick, C. G., Watanabe, Y. W., Wong, C. S., and Yoshie, N.: Evidence for the grazing hypothesis: grazing reduces

- 890 phytoplankton responses of the HNLC ecosystem to iron enrichment in the Western Subarctic Pacific
(SEED II), *Journal of Oceanography*, 63, 983–994, doi: 10.1007/s10872-007-0082-x, 2007.
- Tsuda, A., Takeda, S., Saito, H., Nishioka, J., Nojiri, Y., Kudo, I., Kiyosawa, H., Shiimoto, A., Imai, K., Ono,
T., Shimamoto, A., Tsumune, D., Yoshimura, T., Aono, T., Hinuma, A., Kinugasa, M., Suzuki, K.,
Sohrin, Y., Noiri, Y., Tani, H., Deguchi, Y., Tsurushima, N., Ogawa, H., Fukami, K., Kuma, K., and
895 Saino, T.: A mesoscale iron enrichment in the Western Subarctic Pacific induces a large centric diatom
bloom, *Science*, 300, 958–961, doi:10.1126/science.10820, 2003.
- Ueda, S.: Morphological change of solid ammonium sulfate particles below the deliquescence relative humidity:
Experimental reproduction of atmospheric sulfate particle shapes, *Aerosol Sci. Technol.*, 55, 423–437, doi:
10.1080/02786826.2020.1864277, 2021.
- 900 Ueda, S., Hirose, Y., Miura, K., and Okochi, H.: Individual aerosol particles in and below clouds along a Mt.
Fuji slope: Modification of sea-salt-containing particles by in-cloud processing, *Atmos. Res.*, 137, 216–
227, D17207, doi:10.1016/j.atmosres.2010.10.021, 2014.
- Ueda, S., Miki, Y., Kato, H., Miura, K., Nakayama, H., Furutani, H., and Uematsu, M.: Internal structure of
Asian dust particles over the western North Pacific: analyses using focused ion beam and transmission
905 electron microscopy, *Atmosphere*, 11, doi:10.3390/atmos11010078, 2020.
- Ueda, S., Miura, K., Kawata, R., Furutani, H., Uematsu, M., Omori, Y., and Tanimoto, H.: Number–size
distribution of aerosol particles and new particle formation events in tropical and subtropical Pacific Oceans,
Atmospheric Environment, 142, 324–339, doi:10.1016/j.atmosenv.2016.07.055, 2016
- Ueda, S., Mori, T., Iwamoto, Y., Ushikubo, Y., and Miura, K.: Wetting properties of fresh urban soot particles:
910 Evaluation based on critical supersaturation and observation of surface trace materials, *Science of the Total
Environment*, 811, doi:10.1016/j.scitotenv.2021.152274, 2022.
- Ueda, S., Nakayama, T., Taketani, F., Adachi, K., Matsuki, A., Iwamoto, Y., Sadanaga, Y., and Matsumi, Y.:
Light absorption and morphological properties of soot-containing aerosols observed at an East Asian

- outflow site, Noto Peninsula, Japan, *Atmos. Chem. Phys.*, 16, 2525–2541, doi:10.5194/acp-16-2525-2016,
915 2016.
- Ueda, S., Osada, K., Hara, K., Yabuki, M., Hashihama, and F., Kanda, J.: Morphological features and mixing
states of soot-containing particles in the marine boundary layer over the Indian and Southern oceans, *Atmos.
Chem. Phys.* 18, 9207–9224. doi:10.5194/acp-18-9207-2018, 2018.
- Ueda, S., Osada, K., and Okada, K.: Mixing states of cloud interstitial particles between water-soluble and
920 insoluble materials at Mt. Tateyama, Japan: Effect of meteorological conditions, *Atmos. Res.*, 99, 325–336,
doi:10.1016/j.atmosres.2010.10.021, 2011a.
- Ueda, S., Osada, K., and Takami, A.: Morphological features of soot-containing particles internally mixed with
water-soluble materials in continental outflow observed at Cape Hedo, Okinawa, Japan, *J. Geophys. Res.*,
116, doi: 10.1029/2010 JD015565, 2011b.
- 925 Uematsu, M., Duce, R. A., Prospero, J. M., Chen, L., Merrill, J. T., and McDonald, R. L. Transport of mineral
aerosol from Asia over the North Pacific Ocean, *J. Geophys. Res.*, 88(C9), 5343–5352,
doi:10.1029/JC088iC09p05343, 1893.
- Umo, N. S., Wagner, R., Ullrich, R., Kiselev, A., Saathoff, H., Weidler, P. G., Cziczo, D. J., Leisner, T., and
Möhler, O.: Enhanced ice nucleation activity of coal fly ash aerosol particles initiated by ice-filled pores,
930 *Atmos. Chem. Phys.*, 19, 8783–8800, <https://doi.org/10.5194/acp-19-8783-2019>, 2019.
- Waanders, F. B., Vinken, E., Mans, A., and Mulaba-Bafubiandi, A. F.: Iron minerals in coal, weathered coal
and coal ash – SEM and Mössbauer results, *Hyperfine Interactions*, 148–149(1–4), 21–29,
doi:10.1023/B:HYPE.0000003760.89706.f6, 2003.
- Waller, R. E., Brooks, A. G. F., and Cartwright, J.: An electron microscope study of particles in town air, *J. Air
935 Wet. Pollut.*, 7, 779–785, 1963.

- Wang, R., Balkanski, Y., Boucher, O., Bopp, L., Chappell, A., Ciais, P., Hauglustaine, D., Peñuelas, J., and Tao, S.: Sources, transport and deposition of iron in the global atmosphere, *Atmos. Chem. Phys.*, 15, 6247–6270, <https://doi.org/10.5194/acp-15-6247-2015>, 2015.
- 940 Wiederhold, J. G., Kraemer, S. M., Teutsch, N., Borer, P. M., Halliday, A. N., and Kretzschmar, R.: Iron isotope fractionation during proton-promoted, ligand-controlled, and reductive dissolution of goethite, *Environ. Sci. Technol.*, 40, 3787–3793, 2006.
- Yao, Z. T., Ji, X. S., Sarker, P. K., Tang, J. H., Ge, L. Q., Xia, M. S., and Xi, Y. Q.: A comprehensive review on the applications of coal fly ash, *Earth Sci. Rev.*, 141, 105–121, doi: 10.1016/j.earscirev.2014.11.016, 2015.
- 945 Zhang, D. and Iwasaka, Y.: Nitrate and sulfate in individual Asian dust-storm particles in Beijing, China in spring of 1995 and 1996, *Atmos. Environ.*, 33, 3213–3223, doi: 10.1016/S1352-2310(99)00116-8, 1999.